Fall 2016

In Situ Ion Exchange in a Micro-porous Transition Metal Silicate Framework

Jason M. Lively
Western Kentucky University, jason.lively836@topper.wku.edu

Recommended Citation

Lively, Jason M., "In Situ Ion Exchange in a Micro-porous Transition Metal Silicate Framework" (2016). *Masters Theses & Specialist Projects.* Paper 1730.
https://digitalcommons.wku.edu/theses/1730

IN SITU ION EXCHANGE IN A MICRO-POROUS TRANSITION METAL SILICATE FRAMEWORK

A Thesis
Presented to
The Faculty of the Department of Architectural and Manufacturing Sciences
Western Kentucky University
Bowling Green, Kentucky

In Partial Fulfillment
of the Requirements for the Degree
Master of Science

By
Jason M. Lively

December 2016

IN SITU ION EXCHANGE IN A MICRO-POROUS TRANSITION METAL SILICATE FRAMEWORK

Date Recommended 23 September 2016

Jason S. Polk

Jason Polk, Director of Thesis

Aaron Celestian

Aaron Celestian

Bangbo

Bangbo Yan

David Keeling

11/3/16

Dean, Graduate School Date

ACKNOWLEDGEMENTS

There is a number of people I would like to thank for their help, advice, and support during the completion of this thesis. First, I would like to thank Aaron Celestian for his guidance through the project, his patience with me when I made things difficult, his excitement for his work and, above all else, for treating me as an equal and not just a student. Second, I would also like to thank my committee members, Jason Polk, Bangbo Yan, and David Keeling for their support, not only with this thesis but with hurdles faced along the way. A special thanks to Jason Polk for stepping up to the plate and helping after Aaron started a new career away from WKU (no hard feelings, Aaron, as it worked out well). Next, I would also like to thank Michael May and Nahid Gani for their guidance, aid, and for their problem-solving skills. Finally, I am incredibly appreciative for all the assistance from Wendy DeCroix with paperwork, travel issues, dilemmas in contracts, and all other chaos that comes with the territory.

My gratitude towards the Sponsor Company cannot be fully expressed. Not only was the company willing to allow me to work on this project and to use it for my thesis, but all of those involved were willing to work with me as a colleague, help me whenever it was needed, serve to inspire, and show me that the outcomes of the work would be great. Thanks to this company, my experience, though at times quite difficult, was invaluable.

I would like to express my gratitude to Wenqian Xi at the Advanced Photon Source at Argonne National Laboratory for his help and knowledge with the synchrotron, its operation, and data analysis.

To all of my friends that I have made at WKU, and those from other parts of my journey through life, I cannot thank you all enough, not only for academic support but for all the laughs, adventures, battles, the venting sessions, and for ultimately keeping me sane. Leah Jackson, Dolly Na-Yemeh, Anisha Tuladhar, Indu Bhattarai, Kyle Moss, and Jacob Ruhl – you all made my experience at WKU unforgettable.

I also want to thank my parents, Christina and Michael Lively, my brothers, Nicholas and Brian Lively, my grandfather, Arnold Lively, and the rest of my family for their care, support, and willing ears throughout my academic career.

TABLE OF CONTENTS

LIST OF FIGURES

LIST OF TABLES

IN SITU ION EXCHANGE IN A MICRO-POROUS TRANSITION METAL SILICATE FRAMEWORK

Jason M. Lively December 2016 75 Pages

Directed by: Aaron Celestian, Jason Polk, Bangbo Yan, and David Keeling

Department of Geography and Geology Western Kentucky University

Ion selectivity of minerals has traditionally been utilized in industry as a catalyst, metal separation, and environmental reclamation/sequestration tool. There is an increased interest in understanding ion selectivity mechanisms of micro-porous minerals and mineral-like structures and how they can be applied in various industries: environmental and, potentially, pharmaceutical. This study seeks to understand the ion exchange mechanisms in micro-porous zirconosilicates using time-resolved Raman spectroscopy and X-ray diffraction. The thesis material was exchanged with H^+, Na^+, K^+, and Cs^+ in order to better understand structural changes as well as the influence of the H^+-bonding during the exchange process. It is hypothesized that the host (H^+) ion strongly influences the ion selectivity of the mineral by changing framework polyhedra and ring geometry, and the geometry of the interstitial the $OH \ldots H_2O$ bond network to only allow cations of certain sizes through the channels. In addition, the H^+ may repel cations with high charge densities from entering the extra-framework sites in the crystal structure by protonating the channel pathways.

Chapter 1

Introduction

Application of Ion Exchangers

The understanding of ion exchange within micro-porous materials has been applied in both environmental and industrial fields. Examples of environmental impacts include the purification of drinking water, remediation of agricultural impacts, and removal of heavy metals generated from mining or nuclear reactors (Bortun et al. 1997a; Mumpton 1999; Mishra et al. 2006; Simon et al. 2015). In the chemical and energy industries, exchangeable materials are used to act as catalysts for chemical reactions and for the separation of hydrocarbons (Galadima and Muraza 2015; Góra-Marek et al. 2015; Kumar et al. 2015; Mayani et al. 2015). Recently, the focus is to synthesize minerals to imitate their natural counterparts' sequestering mechanisms and improve their ion sieving properties, in order to increase the application of ion selectivity, including for use in medicine (Anker et al. 2013; Kosiborod et al. 2014; Packham et al. 2014; Stavros et al. 2014; Rafique et al. 2015; Packham and Kosiborod 2015).

Ion Exchange

Ion exchange is process of taking an insoluble solid material that possess ions that can be removed from the extra-framework sites and replaced with another of similar electronic charge distribution. An example is provided in the equations below:

$$2Na^+X^-(s) + 2K^+(aq) \leftrightarrow Na^+K^+X_2^-(s) + Na^+(aq) + K^+(aq) \qquad \text{Eq. 1.1}$$

or

$$2Na^+X^-(s) + 2K^+(aq) \leftrightarrow 2K^+X_2^-(s) + 2Na^+(aq) \qquad \text{Eq. 1.2}$$

An ion exchanging material that has two moles of Na^+ ions, when in a solution of K^+, can exchange the Na for K as an extra-framework ion. The first equation shows that Na and K could occupy the same site and each account for 50%, or they can be completely exchanged. The two Na^+ could also be exchanged with Mg^{2+}, for example, which possesses the correct charge necessary to satisfy the structure and is similar in size. The ion exchange is influenced by more than just charges and one ion can be preferred over the other in the structure based on size, temperature, and structural controls, like protonation and hydration (e.g., Fu and Wang 2011).

Ion Selectivity

Ion selectivity is a preferential inclusion of one ion in a crystalline or molecular structure over one or more other ions. This preferred ion could displace another out of a space in the structure and take its place. The ion's size and charge number influence its desirability in a structure (e.g., the Donnan potential). Similar charged cations are more compatible for ion exchange; for example, two ions with a +1 charge are more likely to exchange than an ion of +1 and +3. The size of an ion also governs exchange; if an ion is too large or small, it cannot properly interact with the framework and will likely be rejected. All systems in nature, and thus in a lab, seek charge balance and ion selectivity is a way to reach that balance in a chemical structure by optimizing ion size and ability to achieve a bond valance sum equal the valance state of the ion. If a mineral with Na^+ present is placed in a solution rich in K^+ (Eq. 1.1 and 1.2), there is an electrical imbalance between the mineral and the solution. This electric potential, known as the Gibbs-Donnan potential, seeks to be resolved. If the mineral is able to spatially accommodate the larger K^+ in its structure and the K^+ more effectively charge balances with the material's framework over Na^+, it will exchange (Helfferich 1962). This is only one possible control on exchange mechanisms and ion selectivity in practice is still not well understood (Lee et al. 2001); however, the precise mechanisms and driving forces that govern ion selectivity are unknown.

In addition to limited knowledge about the mechanisms and controls of ion selectivity in various materials, there is a large gap of knowledge with respect to zirconosilicates. The materials typically studied in ion selectivity are organic compounds and zeolites. Titano- and zirconosilicates are now being further studied for their potential applications. This gap in the knowledge could be from lack of the rarity of the materials, the lack of a need until now, increased technology, or the lack of interdisciplinary work, as these silicates are often studied through a geologic, versus a chemical, lens.

Application of Thesis Material

The application within the scope of this project for ion exchange is the selective removal of K^+ from an aqueous solution. The partial removal of K^+ from living systems is of importance in the pharmaceutical industry for the treatment of hyperkalemia, which is a condition involving above normal $[K^+]$ in the blood stream. The ideal material used to trap K^+ must prefer to absorb K^+ into its structure over other competing elements, such as Na^+, Mg^{2+}, or Ca^{2+}. The material under study can be considered a part of the porous heterosilicate family, a group of minerals with zeolitic-like properties. A zeolite is a micro-porous aluminosilicate mineral often used as an absorbent in industrial applications. These groups of mineral-like structures are highly ion selective and have been utilized in a wide variety of applications (e.g., Bortun et al. 1997b; Mishra et al. 2006; Pang et al. 2007; Uguina et al. 2008).

The material under evaluation is the full sodium form of the zirconium silicate (material #1) and is capable of selectively sequestering K^+ from aqueous solutions (Anker et al. 2013; Stavros et al. 2014). A variation of this material was studied in human clinical trials in hyperkalemic (>5.1 mEq/L of K in blood) patients (Anker et al. 2013; Packham et al. 2014; Kosiborod et al. 2014; Packham and Kosiborod 2015). In clinical trials, the test article was shown to take the amount of K^+ in the blood back to healthy levels within two hours and maintaining normal potassium (3.5 to 5.0 mEq/L of K in blood) for 24 hours and beyond with the appropriate dose. Patients were given various amounts of the agent/drug as a powder: placebo group, 5 g, 10 g, or 15 g a day for 28 days. Approximately 90% of the patients that received the test article reached normokalemia. Some patients in the group that had taken 15 g for the duration of treatment experienced some hypokalemic (<3.4 mEq/L of K in blood) levels (Anker et al. 2013) that were quickly restored to normal potassium after suspending dosing or the reduction in dose. Other clinical studies also found the compound to be effective (Packham et al. 2014; Rafique et al. 2015; Packham and Kosiborod 2015).

The effectiveness of the test material toward selective absorption of K^+ is compared to a synthetic organic resin that is currently used to treat hyperkalemia, but the resin is known to absorb other electrolytes in addition to K^+ (Watson et al. 2010; Packham and Kosiborod 2015). This resin material is problematic, because it is not ion selective, thus taking all cations from an electrolyte without preference and having potentially low efficiency to fully treat hyperkalemia, if exchange sites in the resin are used up by non-K^+ ions.

Summary of Structure – Material #1

Material #1 ($Na_2ZrSi_3O_9 \bullet 2.5H_2O$) is the as-synthesized parent material to the other two used in this study. Material #2 ($\sim HNaZrSi_3O_9 \bullet 2.8H_2O$**)** and material #3 ($H_{1.3}Na_{0.7}ZrSi_3O_9 \bullet 3H_2O$) are more protonated forms of the material #1. The overall structures are arranged similarly, however, the bond distances and void spaces vary in size between the three different forms. Material #2 and material #3 will be discussed in greater detail in Chapters 3 and 4, respectively. Material #1 and material #2 were kindly provided by the Sponsor Company. The material is made up of 7MRs (Figure 1.1), 3MRs (Figure 1.2), and 6MRs (Figure 1.2).

The chemical formulas for each of the three forms were calculated. Due to complications with the disorder among extra-framework sites, these formulas are approximations of the site occupancies. The H_2O content for each material was determined by thermogravimetric analysis; however, more robust techniques for chemical determination are necessary for a more precise description of the chemical formulae (e.g., XRF and/or ICP-OES).

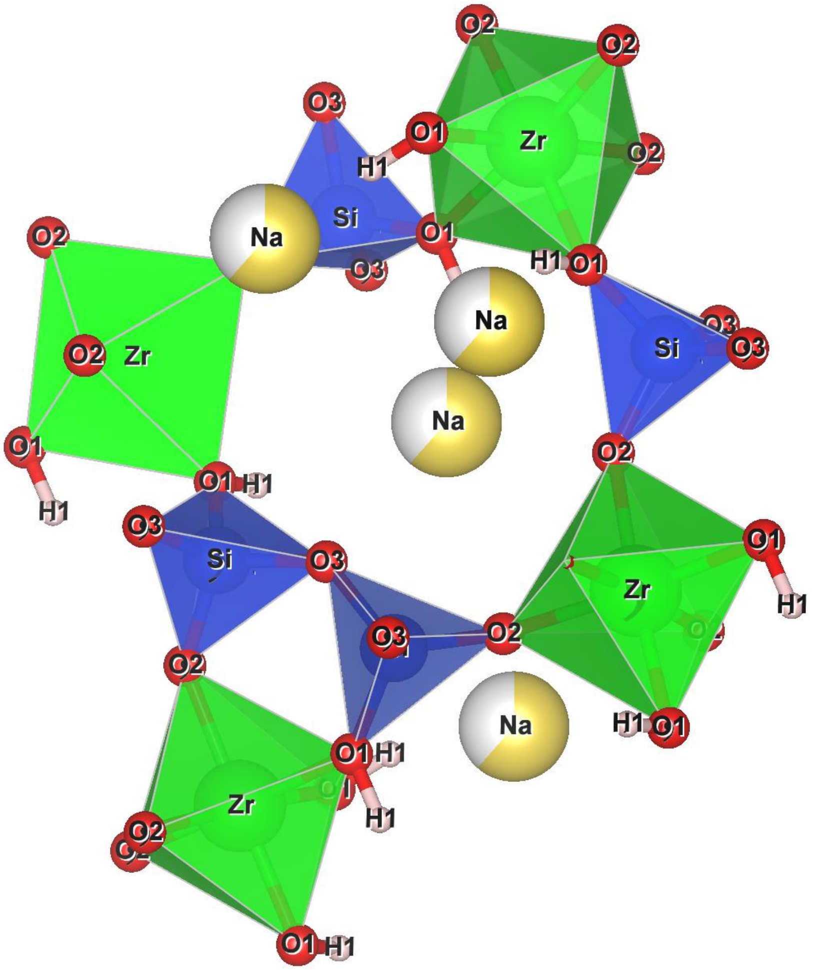

Figure 1.1 Model shows material #1 with Na in the center of the 7MR openings to the cage. One 3MR is shown at the bottom of the figure (Si1-O2-Zr1-O3-Si-O1). Na cations are all located in the center of the 7MR, where the 7MR is the confining ring for access to the cage. Note that the calculated positions of the OH hydroxyl group points into the 7MR. Source: Created by the Author.

Figure 1.1 is a crystallographic model of the material #1 7MR structure created in VESTA (Momma and Izumi 2011). The Na^+ site is in the center of the 7MR with a Na to framework O bond length of 2.59 Å. The 7MRs are the confining ring opening that connects the structural cages (Figure 1.3). The 7MR (Figure 1.1) is comprised of four SiO_4 tetrahedra and three ZrO_6 octahedra with a long-axis and a short-axis of 6.5 Å and 5 Å respectively. The shortest distance in material #1 is between sites O3…O1. This

O3…O1 distance is shorter in material #2's structure as the H1 sites form hydroxyls on O1 resulting in an O3…H1 distance of 4.2 Å. The 3MR is formed by two SiO_4 tetrahedra and ZrO_6 octahedra (Figure 1.1). The 3MR does not contain any extra-framework cations, but is a structural building unit that forms the larger 6MR, 7MR, and cages.

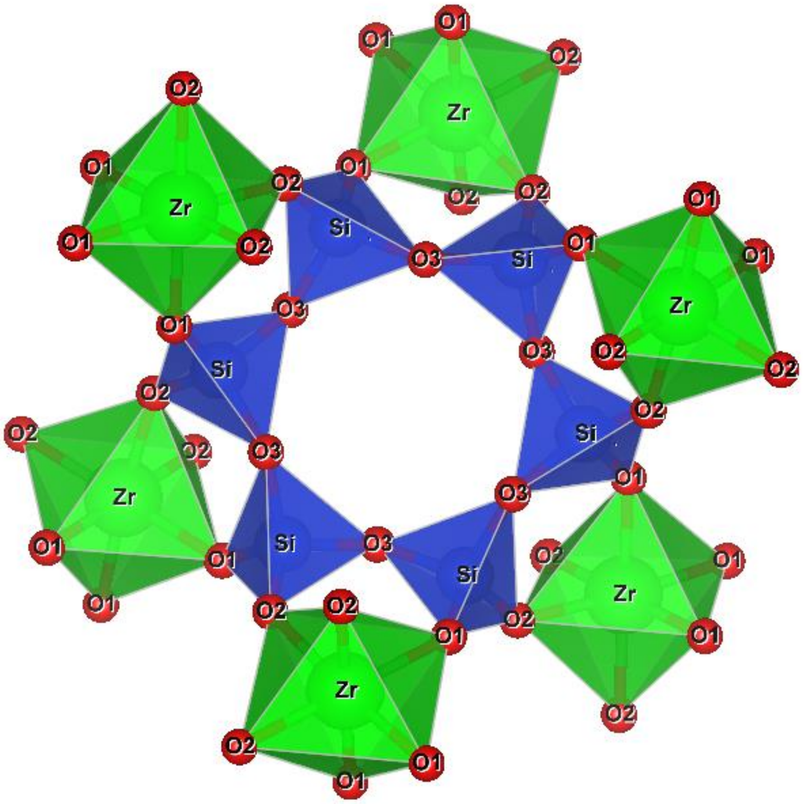

Figure 1.2 Model illustrates the research material's 6MR is formed by three 3MRs. Source: Created by the Author.

The 6MR (Figure 1.2) in the test material is solely composed of SiO_4 forming rings of composition Si_6O_{18}. The centers of these 6MR do not contain extra-framework cations. Of the three different rings that comprise the crystal structure, only the 7MR contains extra-framework cations and act as a gateway between channels and the structural cages.

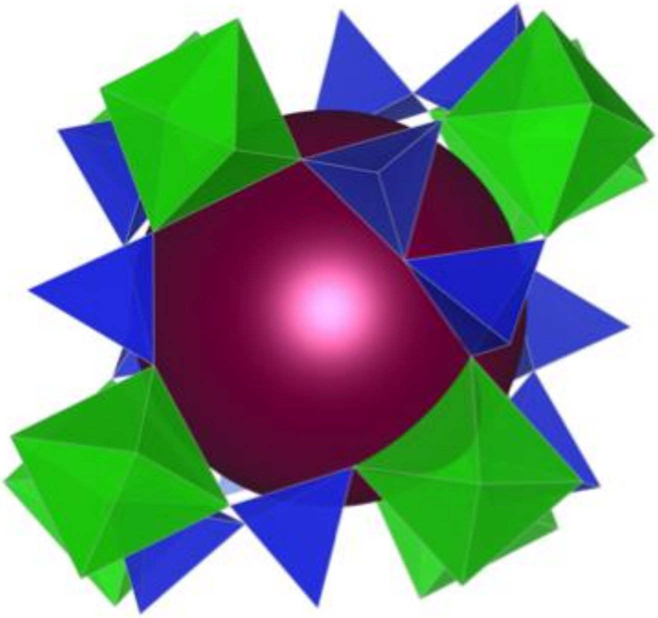

Figure 1.3 Model shows the structure of the thesis material showing the cage structure and its volume (purple sphere) is found to be approximately 18 Å^3. The 7MR and connecting 3MR are shown. O and the central cations of the polyhedra have been removed for clarity. Source: Created by the Author.

The cage structure (illustrated by the purple sphere) and channel openings are formed by the intersection of the 7MRs (Figure 1.3). The cage is a site that can potentially trap ions larger than Na$^+$; therefore, the crystallography and crystal chemistry of the cage is important to consider as a potential site for K$^+$ and other ions.

The 7MR confines the channel pathways where ion exchange occurs. In the center of the 7MR ring, the ions are in a 6-fold coordination geometry. The ionic radius of Na$^+$ and K$^+$ in a 6-fold coordination are 1.02 Å and 1.38 Å (Shannon and Prewitt 1969), respectively, with an O-Na-O length of 4.74 Å and an O-K-O 5.46 Å (values obtained using VESTA and encipher (Jones et al. 1997)). The 6-fold coordination geometry for extra-framework cations is used as a proxy for modeling ion exchanges within the crystal framework. The ionic radius of the larger monovalent cation, Cs^+, in 6-fold coordination is 1.67 Å (Shannon and Prewitt 1969), with a calculated O-Cs-O of 6.04 Å. Due to size constraints of the 7MR (long-axis and short-axis of 6.5 Å and 5 Å, center–center distance, respectively), the K^+ ion may represent the largest cation that can pass through the 7MR channels without distorting the crystal structure. In order for Cs^+ to pass through the 7MR and into the cage, the structure would need to change geometry to accommodate the large Cs cation.

Overview of Results

The research materials are originally synthesized as a Na^+ framework zirconium silicate, and were previously shown to be effective sieves for K^+ ion exchange (Stavros et al. 2014). In material #1, the Na^+ is readily exchanged for K^+. Time-resolved X-ray Diffraction found that the K^+ occupies the Na^+ site, though it is unable to fully expel all of the Na^+. Material #1, after having been exchanged with K^+, was exposed to 1.0 M NaCl solutions, and showed Na^+ would not back-exchange K^+ out of the structure. In material #1, Cs^+ represents larger cations and was able to be exchanged; however, it caused larger distortions in the structure than the smaller monovalent ions and occupied a site in the cages.

Material #2 and material #3, which represent different amounts of protonation of the framework, also show a preference to the K^+ ion. The protonation of material #1 to yield material #2 and material #3 causes the unit-cell to increase in size, increases the 7MR diameter allowing the ions to pass more easily through the channels. The opening of the 7MR is caused by the elongation of the Zr-OH bond, yielding an increased volume of the ZrO_6 octahedra. In the parent material (#1), the walls of the channel pathways are negatively charged due to the surface being composed of O^{2-}. As the material is protonated the negative channel pathway has areas of positive charge, and decreases the size of the channel due to elongation of the ZrO_6 octahedra. Large cations and high charge density cations are likely repelled form the structure due to these positive charges in the channel. The O-H molecules formed during protonation likely form strong covalent bonds and this bond energy would need to be overcome to allow cation exchange to occur. The protonation of the research materials yields a rapid initial uptake of the K ions into the framework. The amount of K sequestered by material #1, material #2, and material #3 is approximately the same between the three materials; however, the rate of uptake varies.

Alongside the protonation effect, there could also be an extra-hydration influence in the channels. The maximum hydration observed was for research material #3. Thermogravimetric Analysis of material #1, material #2 and material #3 shows that H_2O is a key part of the materials structural stability at high temperature. While material #1 and material #2 remained similar to their original structure, material #3 became amorphous at high temperatures, suggesting that either the hydration effect is an important process, or the small ionic radii of H^+ is not large enough to support the structure after dehydration. In order to evaluate the role of hydration, neutron scattering studies would be necessary to model H_2O and OH positions in the crystal structure as a function of ion exchange and temperature. The neutron study is not a part of this project.

Chapter 2

Ion Exchange processes in $Na_2ZrSi_3O_9 \bullet 2.5H_2O$ – Material #1

Introduction

Material #1 is the parent material to the others discussed through this study. It is the most actively used form by the Source Company and the primary material used in this study. Material #1 does not yet have a natural mineral counterpart that has been found to exist. Chemically, it is similar to a number of zirconosilicates, but its structure is unique in that it is a ring silicate and has the 7MR and 3MR comprised of both ZrO_6 and SiO_4 polyhedra.

Material #1 was exchanged with H^+, Na^+, K^+, and Cs^+ in this study to understand the exchange process and mechanisms involved during ion exchange. It is important to understand the crystal chemical and molecular processes that enable the structure to have an affinity towards K^+ over the other monovalent cations, as well as a reason for the rejection of higher valence cations. Material #1 exchanged with H^+ ions results for the production of material #3, which is detailed in Chapter 4. The other cation exchanges tested the restrictions and role size in the exchange process, and if the structure would accommodate large ions.

Methodology

Ion Exchange

The ion exchange was carried out via a flow through cell so that the materials would be exposed to a constantly refreshed solution to minimize any effects of local exchange equilibriums. The flow rate of the exchanging solution was held constant for the entirety of the experiment by means of a peristaltic pump (Celestian et al. 2013).

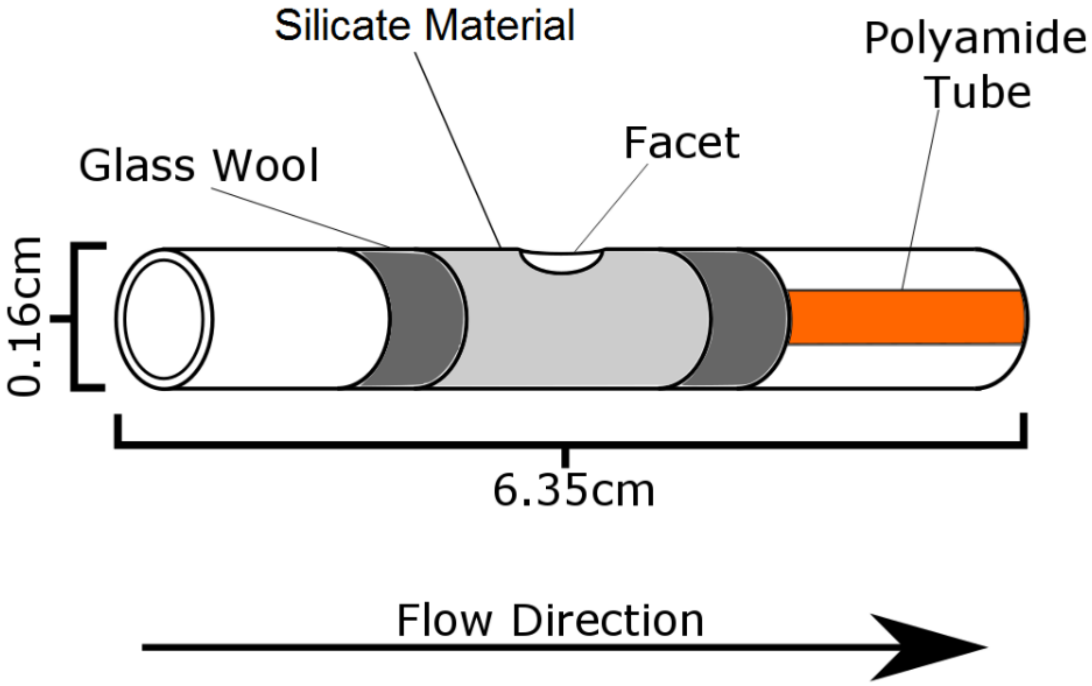

Figure 2.1 The design of the sapphire cell for time-resolved Raman Spectroscopy studies. Source: Created by the Author.

The sapphire cell (Figure 2.1) was constructed for this study and utilized during the time-resolved Raman experiments. In the sapphire wall, a lens is ground (2mm by 1mm) to allow the beam from the Raman spectrometer to interact with the material with less absorption by the sapphire, and the lens acts as a condenser to redirect some of the Raman back-scattered light into the objective. The material was in the center of the cell seen in light grey. On either side, in dark grey, there was glass wool to prevent the material from moving as the solution was pumped through. The polyamide tube seen in orange was used as a spacer and support rod to keep the material in place. The flow direction, as noted in Figure 2.1, is from left to right. The connector that attached to the right side of cell acts as a barrier to prevent movement, but allows the solution to flow. The flow rate was set to a value of 0.4 (unit-less value) on the peristaltic pump, which yielded a flow rate of approximately 0.05 mL/min.

Table 2.1. The resultant materials of ion exchange studies.

Original Material	Ion Exchange	Resulting Material
#1	H^+	#3
	K^+	#4
	Cs^+	#6
#4	Na^+	#5

Source: Created by the author.

Hydrogen

In *in-vitro* experiments, material #2 was found to exchange K^+ at a slower rate than material #1. The slower exchange rate suggests that the H^+ influences the rate of the exchange process. To evaluate the rate of exchange, and any influence of the H^+, material #1 was protonated with a 0.01 M HCl solution (yielding material #3). The solution was made by adding 0.82 mL of 12.1 M HCl to 1 L of deionized H_2O. The material #6 material was then exchanged with 0.01 M KCl, 0.01 M NaCl, and 0.01 M CsCl solutions to evaluate any differences in the time-resolved Raman spectra, and identify the role of H^+ in the ion exchange process by evaluating our structural models for changes in bond lengths and bond angles.

Potassium

The materials, #1, #2, and #3, are thought to be highly selective of K^+ ions. In order to verify this, and to understand the structural changes that occur as K^+ ion exchange takes place, the ion exchange was done by flowing a 0.01 M solution of KCl through the cell. The solution was made by adding 0.74 g of KCl (s), 99^+ % purity, to 1 L of deionized H_2O.

Cesium

Cs is a monovalent cation like K^+, Na^+, and H^+. The Cs^+ ion is larger than K^+ by 0.29 Å. The intent of ion exchanging material #1 with Cs^+ is to identify the changes in the crystal structure to accommodate these ions and the rate at which this occurs. The Cs^+ would have to distort the structure in order to pass through the ion channels. The solution was made to be 0.01 M, which equates to 1.68 g of CsCl (s), 99.99 % purity, to 1 L of deionized H_2O.

Sodium

To evaluate any issues with back exchange, a 0.1 M solution was made by adding 5.8 g of NaCl (s), 99^+ % purity, to 1 L of deionized H_2O. If there is a possibility of Na back exchange into material #3, the higher Na concentration should be able to force that process, increasing the Donnan potential in favor of Na in this system (Helfferich 1962).

Raman Spectroscopy

Data from time-resolved Raman spectroscopy studies are used to model the molecular distortions and changes taking place to the bonds within the material during ion exchange. Raman spectroscopy is ideal for modeling local changes to bond geometry. The Raman spectrum is generated by the Raman Scattering and Stokes scattering electrons. These electrons are excited by the beam and change vibrational state (Masters 2009). It is not an orbital jump that would release greater energy (e.g., fluorescence), but a small virtual energy change that exists from the bending and moving of bonds within the crystal structure. Changes in the Raman shift generated by the structural changes have been measured and analyzed for similar materials (e.g., Celestian et al. 2013) and atomic structural models derived from this study help to reveal exchange pathways of in-going cations. The Raman spectra were fit using MagicPlotPro to evaluate the structural changes and kinetics of ion exchange within the material.

The time-resolved Raman studies were performed using a DXR Raman Microscope with a 780 nm near infrared laser. The analysis was set to 10 sec exposures three times for a total of a 30 sec scan, or frame. There was a total of 400 frames, which yields approximately a 3.3 hour timespan over which data were collected to track the changes Raman spectrum through time.

X-ray Diffraction

X-ray diffraction (XRD) was also required to determine the crystal structure and cation migration during the ion exchange process. XRD utilizes the energy from X-rays to generate a pattern of energy release at discrete diffraction angles (Bish and Post 1989). The diffraction pattern is characteristic of the atomic structure that is interacting with the X-rays. XRD is effective for modeling long-range atomic arrangements, chemical site occupancies, and structural configurations. Time-resolved XRD is a specialized technique where the crystal structure can be modeled at every time-step of the exchange process, thus revealing atomic motion during the diffusion events. Ideally, fast data collection will yield the best results, where slow data collection tends to give overlapping positions of the difference Fourier transform (essentially making blurry images of the atomic arrangement); therefore, synchrotron radiation was used to obtain the required high flux of X-rays for rapid data collection (e.g., Celestian et al. 2013). Structural models were developed using the Rietveld refinement implemented in the GSAS-II software (Toby and Von Dreele 2013).

The time-resolved X-ray synchrotron diffraction (XSD) studies were performed at the Advanced Photon Source Synchrotron, a part of the Argonne National Laboratory. The synchrotron provided the high-flux X-ray source needed to collect rapid data necessary for successful time-resolved work. The XSD studies were carried out using a similar cell design as the sapphire cell (Figure 2.1), but it was made of polyamide tubing rather than sapphire glass. The single crystal sapphire would strongly scatter X-ray, a thus causing over-saturation problems on the X-ray detector. Polyimide tubes weakly scatter X-rays; therefore, it is a more desirable material for XSD work. Utilizing the XSD beam with a 0.72768 Å wavelength, the diffraction pattern acquisition was set to 0.5 sec exposure 20 times for a total of a 10sec/scan, or frame. The beam shutter closed for 20 secs (total 30 secs per scan) to remove any residual diffraction images (i.e. ‘ghosting’) from the detector. There were a total of 400-1000 frames in each experiment to evaluate structural changes through time.

Thermogravimetric Analysis

H_2O is a significant constituent of the research materials and understanding its role during the exchange process was necessary for a full evaluation of the ion exchange mechanisms. The mechanism for ion exchange was previously thought to be a combination of an effect due to the hydration shell of the extra-framework ions and protonation of the materials (Stavros et al. 2014). To evaluate the extent of hydration of the protonation of the material, thermal analysis of material #1 was performed with a Netzsch STA 449 F1 Jupiter with TGA and DSC analyzers. Approximately 10 mg of the material was heated to 600 ºC at 1 ºC/min in air. The analysis illustrated weight loss due to H_2O evaporation. After the TGA analysis of material #1, it was analyzed via a Rigaku MiniFlexII Desktop Powder X-ray diffractometer to evaluate any major structural changes in the material.

Results

Raman Studies

The Raman spectrum for material #1 is seen in Figure 2.2. There are a series of peaks noted in the spectrum at varying Raman shifts, although all peaks were measured and analyzed, it was determined that the primary focus of the study is the v5 peak found at 520 cm^{-1}. This peak was found to be representative of changes in the geometry of the 3MR (Figure 1.2 to 1.3). The 417 cm^{-1} and 645 cm^{-1} peaks are representative of the sapphire used to calibrate and account for changes in the Raman laser frequency. The peaks around 900 cm^{-1} are characteristic of SiO_4 stretching modes. The v5 peak at 520 cm^{-1} showed measurable change during the exchange process whereas the other peaks did not. The v5 peak is discussed in each of the exchanges later in this section.

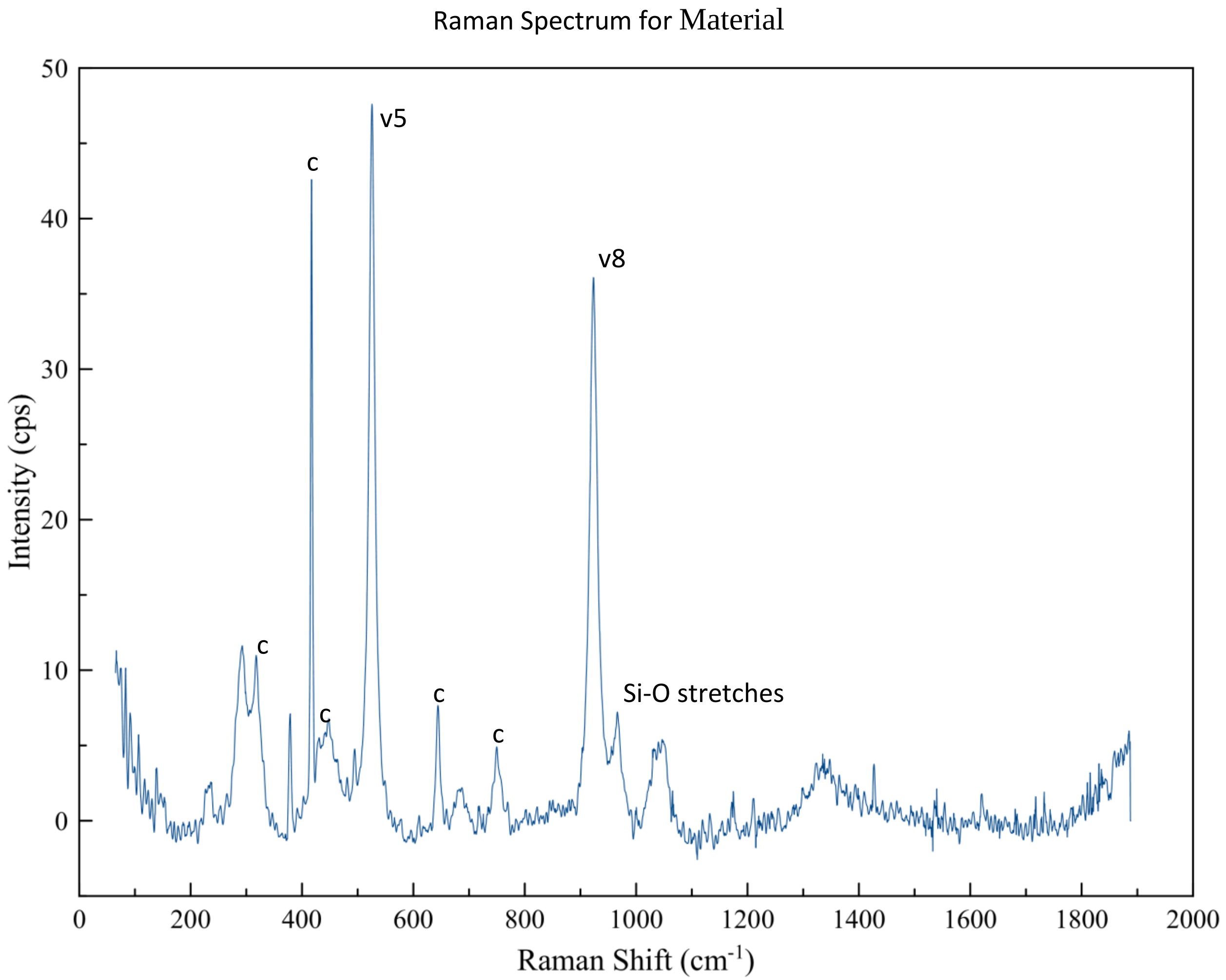

Figure 2.2 Graph showing the Raman spectra for the material #1, the Na-form, parent material. “c” refers to sapphire peaks. Source: Created by the Author.

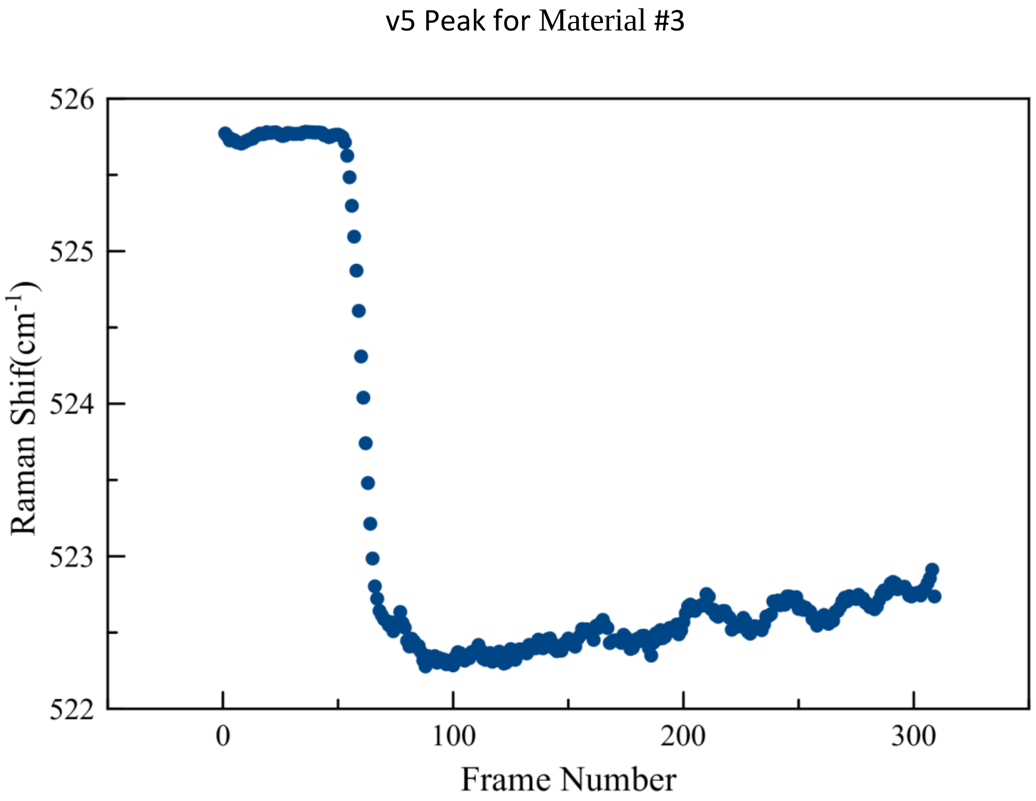

Figure 2.3 Graph showing the change in the v5 peak, which signifies distortion of the 3MR during protonation of material #1. Source: Created by the Author.

Figure 2.3 shows the time-resolved Raman shift for changes in the v5 peak of material #3. Material #3 is the maximally protonated form of material #1. As H^+ enters structure it causes the 3MR geometry to stretch to higher wave numbers suggesting that the 3MR bonds are being distorted, and the 3MR is becoming locally strained and less symmetric. Each frame number equates to approximately 35 secs of real time. The exchange begins at frame 30 and completes by frame 80. Protonation of the thesis material is rapid, requiring only 29.2 minutes. The positive trend seen in Figures 2.3 and 2.4 is due to shortening of the Zr-OH bonds as exchange occurs.

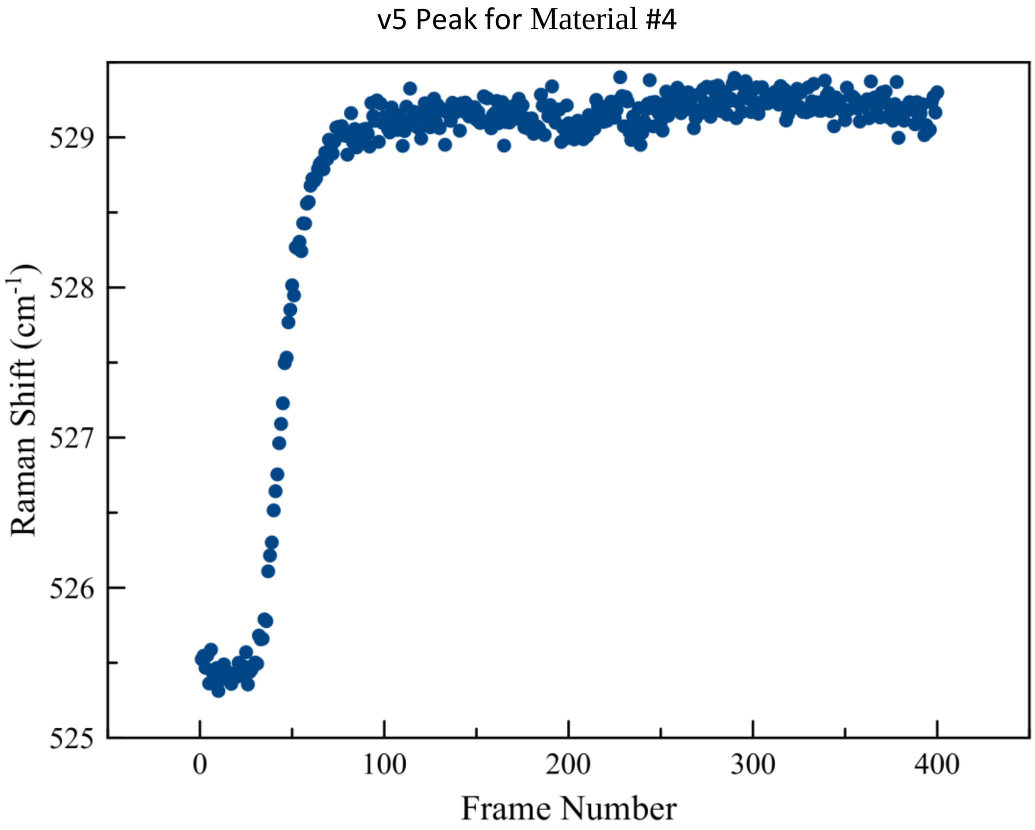

Figure 2.4 Graph showing the change in the v5 peak position during the K$^+$ exchange into material #1. Source: Created by the Author.

Figure 2.4 shows the time-resolved Raman data for the v5 peak in the material #1 to material #4 exchange (Na$^+$ to K$^+$). Material #4 is the K$^+$ form of material #1. As the K$^+$ ions move into the crystal structure, there is a shift to higher wave numbers in the 3MR peak. The exchange of K$^+$ into material #1 occurs from frame 15 to just past frame 100. Exchange in this experiment reaches near completion within an hour.

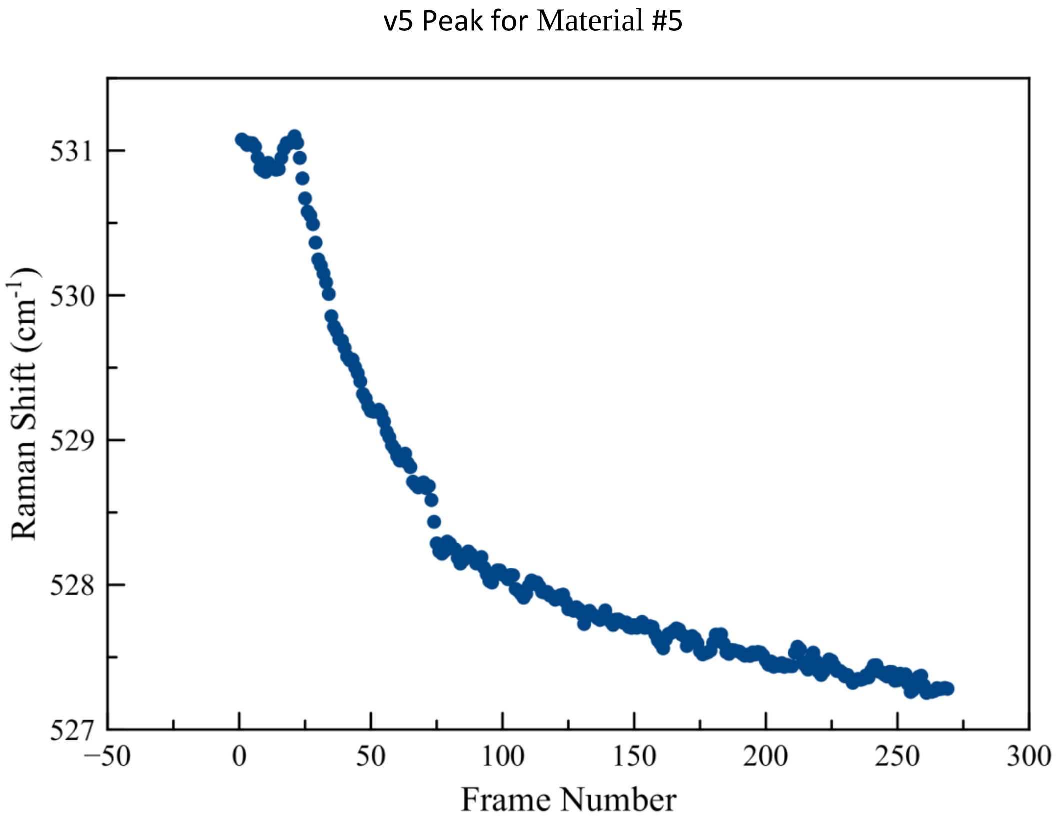

Figure 2.5 Graph showing the change in the v5 peak position as Na$^+$ is back exchanged into material #4. Source: Created by the Author.

The goal of the research material is to show affinity towards K$^+$ over other ions. Material #5 is used to evaluate any back exchange between extra-framework cations. Na$^+$ is the original host cation. Figure 2.5 shows the exchange of Na$^+$ into material #4 yielding material #5. The v5 peak is seen to shift towards lower wave numbers. The trend shows that Na$^+$ does back exchange in the presence of K$^+$, in the minimally protonated material #1 protonated material. The peak shifts back towards the initial position, but does not shift all the way to 525 cm^{-1}, suggesting that not all of the K$^+$ is exchanged out.

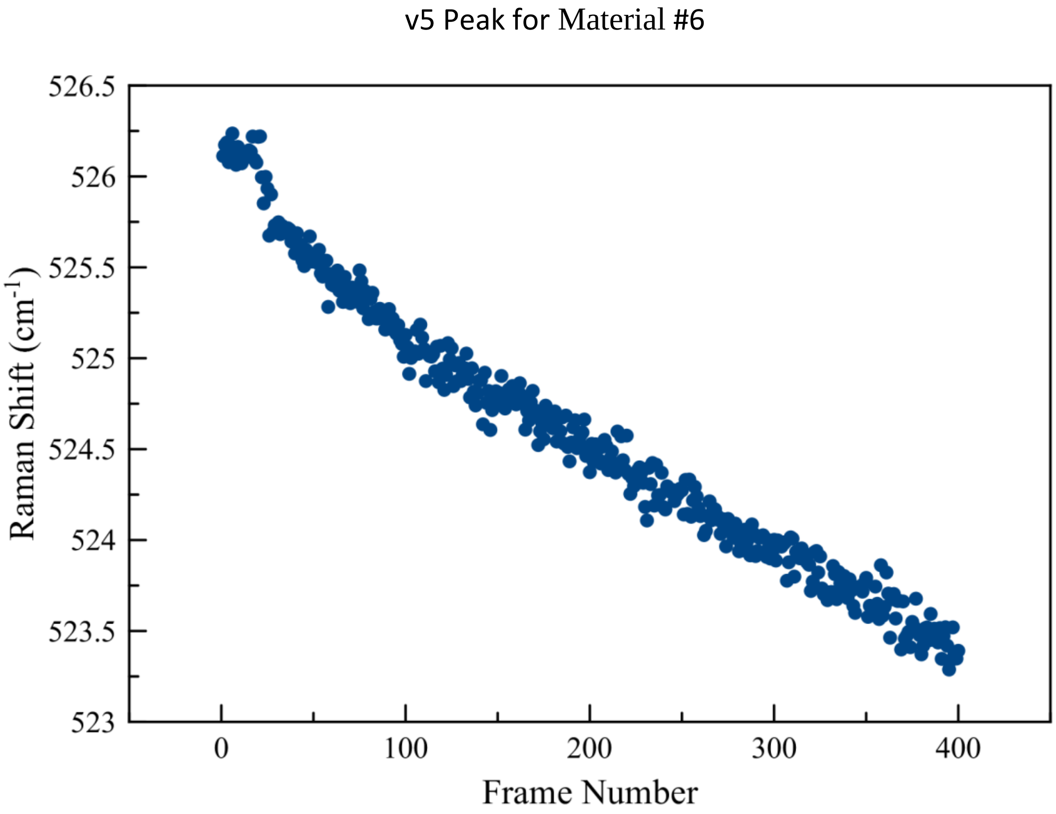

Figure 2.6 Graph showing the change in the v5 peak position as Cs$^+$ is exchanged into material #1. Source: Created by the Author.

Figure 2.6 shows the trend of the Cs$^+$ exchange into material #1 yielding material #6. As Cs$^+$ enters the channel pathways and enters the crystal structure, it causes the 3MR geometry to shift towards lower wave numbers. The trend appears to be linear, but at a slow rate in comparison to the exchanges seen in Figures 2.3 to 2.5. The negative trend in the shift is due to elongation of the Zr-OH bonds. It takes 400 frames to achieve a 3 cm^{-1} shift. Exchange does not reach completion in the 4.5 hours of exchange.

XSD Studies

The XSD studies are time-resolved experiments completed at the APS. Due to time constraints, not all of the Raman experiments were recreated. The exchanges performed with material #1 were the protonation (Figures 2.7, 2.10, and 4.6) and K^+ exchange (Figures 2.8, 2.9, and 2.11). Material #3, the protonated form, is briefly mentioned in this chapter, but see Chapter 4 for more detail.

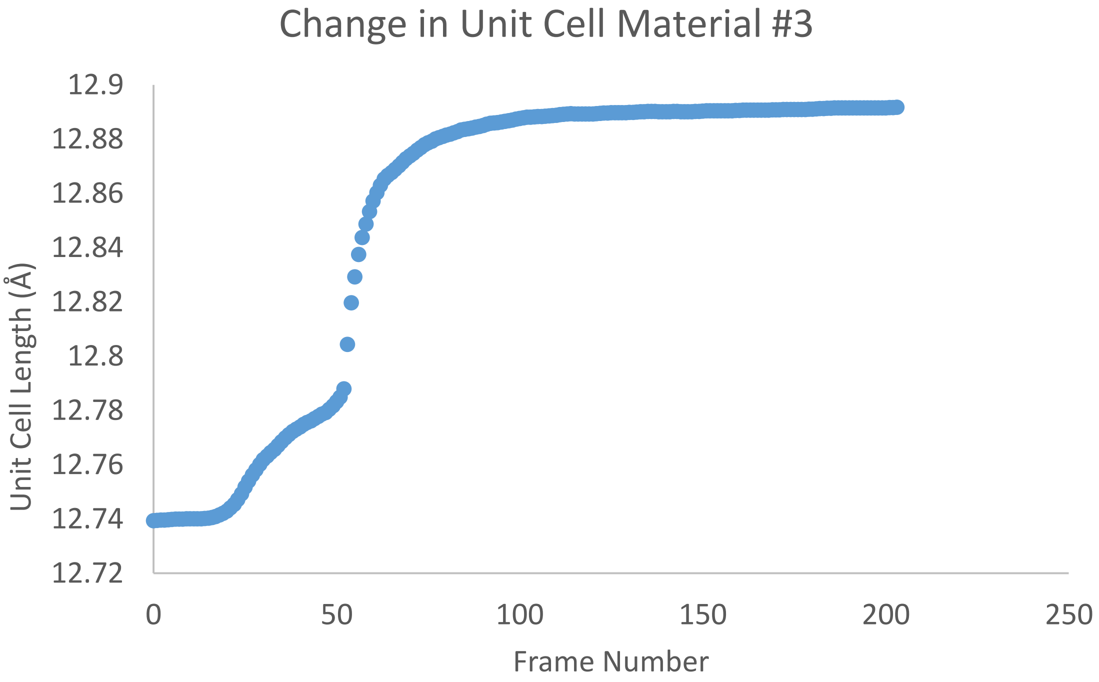

Figure 2.7 Graph showing the change in the unit-cell length as material #1 is protonated to yield material #3. The plot is comprised of individual points and is not a trend-line. Source: Created by the Author.

The structure of material #3 is discussed in Chapter 4 in greater detail, but it is shown in Figure 2.7 that the unit cell increases in size as exchange occurs. There is a two-step process. The first step is seen between frames 25 and 60, and the sec step from 60 to 100. The first step allows for much more rapid uptake of H^+ relative to the first seen by an increased rate of change. The total change in the unit-cell length is 0.150 (1) Å.

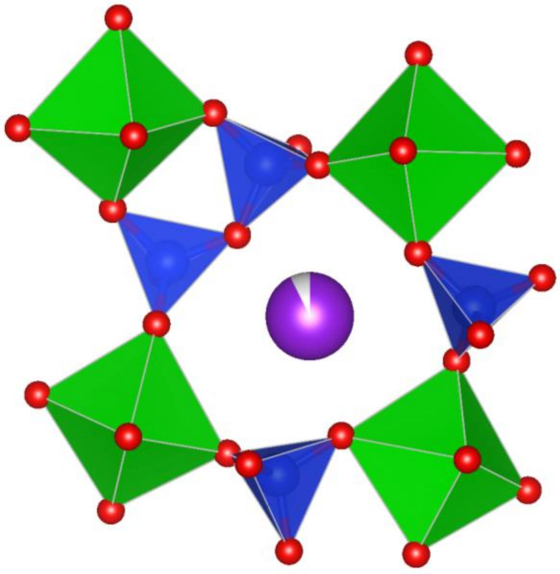

Figure 2.8 Model shows the structure of material #4, with K^+ located at the Na^+ site of material #1, inside the 7MR. Source: Created by the Author.

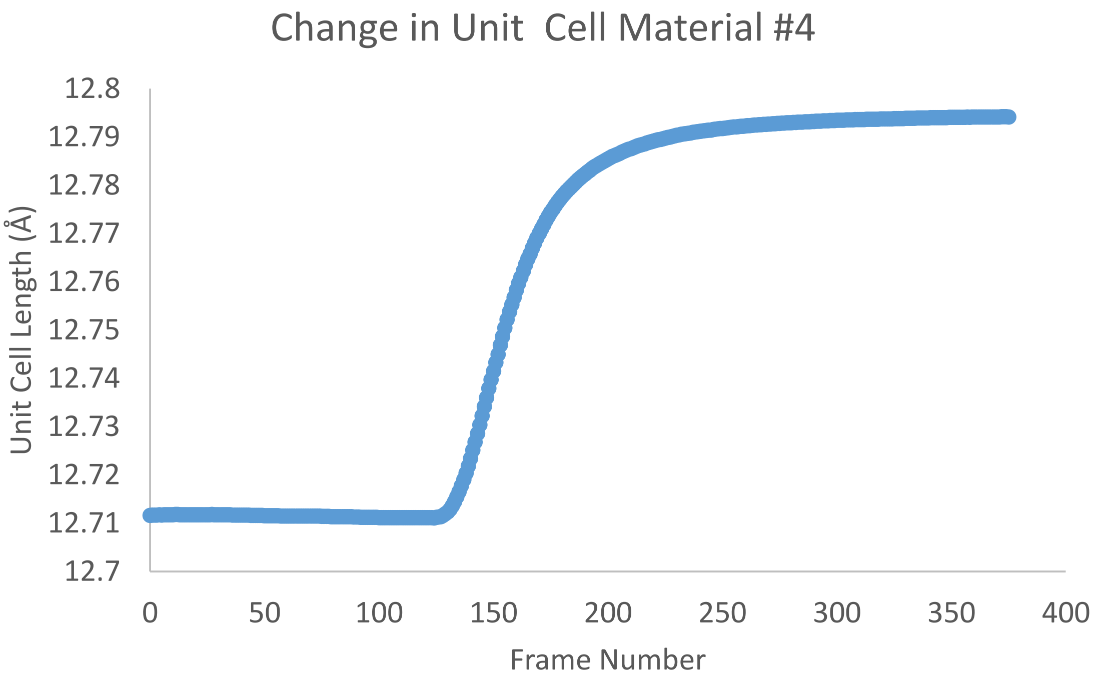

Figure 2.9 Graph showing the changes to the unit-cell length in material #4. The plot is comprised of individual points and is not a trend-line. Source: Created by the Author.

The XSD results of the K^+ ion exchange into material #1 indicate there is an increase in the size of the unit-cell of the material seen in Figure 2.8 and 2.9. Figure 2.8 shows a representation of the structure after it has been maximally exchanged with K^+. There is slight distortion, which is shown by the unit-cell size increase. The unit-cell increases 0.9000 (9) Å in length. The structural refinements of the XSD data illustrated that the K^+ ion resides in the same site as the Na^+ ion. The extra-framework site has a 33% chance of Na^+ occupying the site and a 67% chance of K^+ occupying the site. The positions and occupancy of H_2O were evaluated and represented as O ions (Ow), which are not represented in Figure 2.8, as it also partially occupies sites that surround the monovalent cations and is also in coordination with the framework. On either side of the cations in the 7MR window, there is an Ow site.

The 3MR showed the largest amount of distortion during the exchange of both cations. The 3MR is made up of two SiO_4 and one ZrO_6 polyhedra. The O distances represent the stretching and shortening of the SiO_4 tetrahedra. O1 and O2 are O atoms that link the SiO_4 and ZrO_6 together, O3 links two SiO_4 tetrahedra. Figures 2.10 and 2.11 (material #3 and material #4 respectively) show the variance in the distance between these O atom bonds through time. The O1…O3 is longer than that of the O2…O3. The ratio between the two reveals if one side of the SiO_4 is being distorted faster than the other. The 3MR dihedral angle was also modeled through time. The dihedral angle (Zr-O2-Si-O3) is a measure of dihedral resulting from a twisting of the 3MR, which corresponds to the changes in the v5 peak in the Raman analysis.

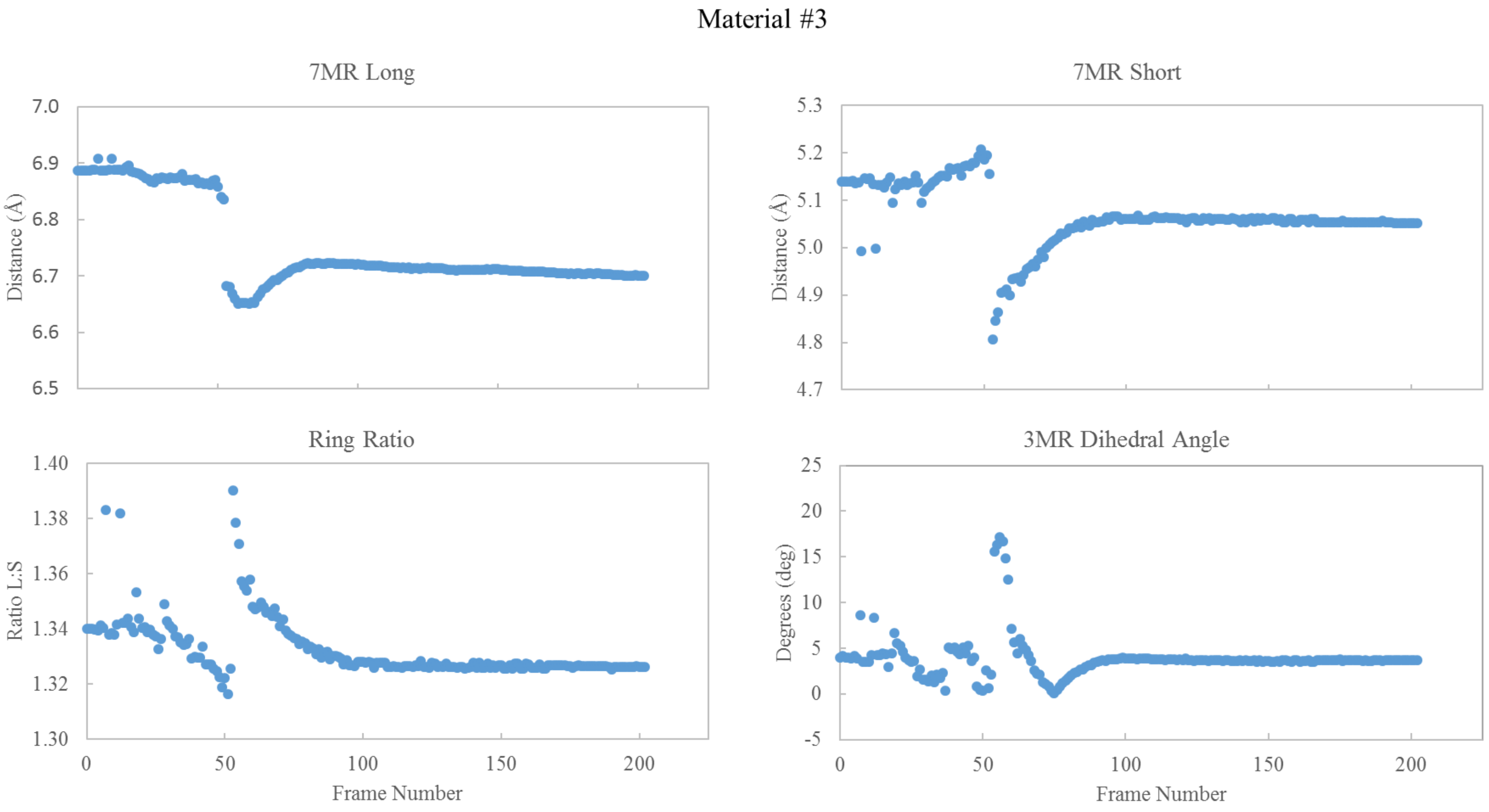

Figure 2.10 Plots represent the changes in O…O distances; O1…O3 (upper left), O2…O3 (upper right), ratio of the O1…O3 and O2…O3 bond distances (lower left) and the changes in the dihedral angle of the 3MR (lower right) in material #3's sequential synchrotron data. Source: Created by the Author.

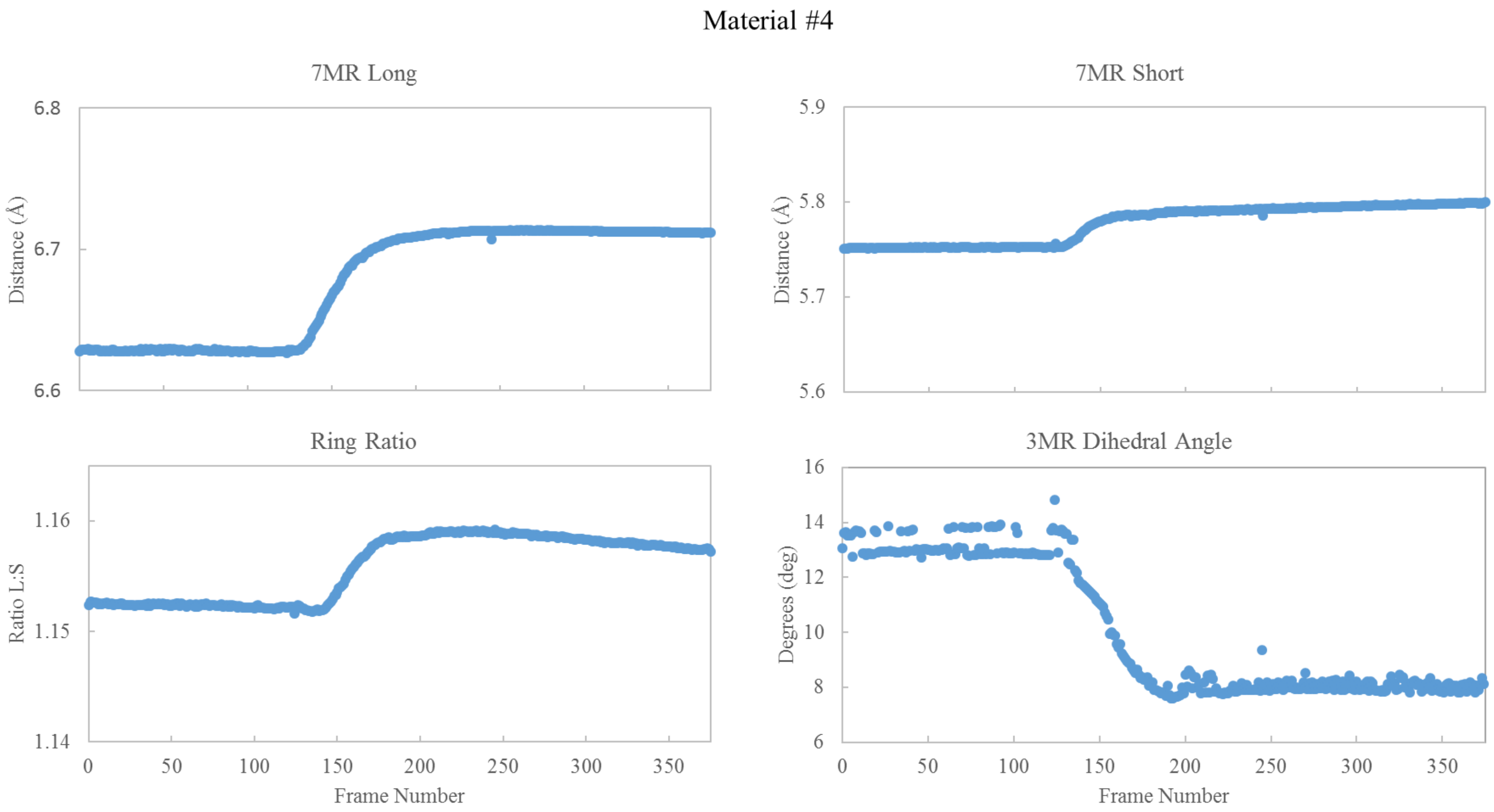

Figure 2.11 Plots represent the changes in O…O distances; O1…O3 (upper left), O2…O3 (upper right), ratio of the O1…O3 and O2…O3 (lower left) and the changes in the dihedral angle of the 3MR (lower right) in the material #4's sequential synchrotron data. Source: Created by the Author.

In the resultant material #3 (Fig 2.10), the long and short O distances shortened overall as exchange occurred. The ratio between the two distances remains fairly constant, but does show that the O2…O3 shortens slightly faster than the O1…O3, due to a slight decrease in the ratio between them. The dihedral angle fluctuates during the stages of exchange, but settles down at about frame 100, same as the change in the unit-cell. Ultimately, as exchange completes the distortion angle remains the same as it was at the beginning.

In material #4 (Figure 2.11), both of the long and short distances lengthened, with a larger increase in the O1…O3, as seen in the ring ratio. The change in the distance in both cases is on the order of 0.1 Å. The dihedral angle in material #4 distorts 6º.

TGA Study

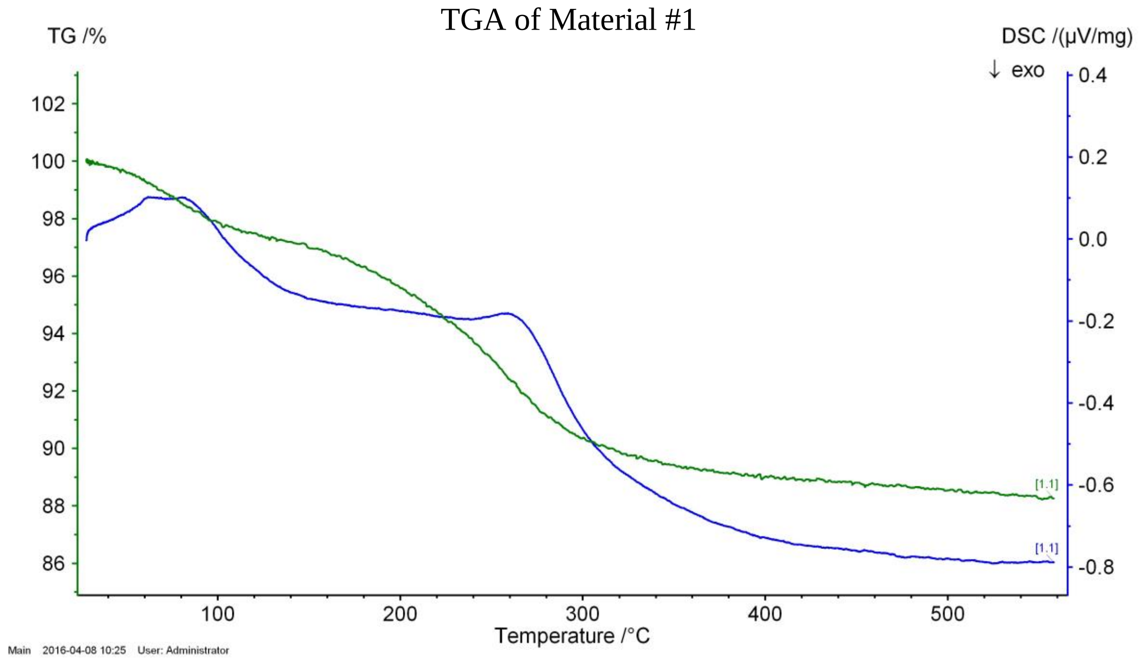

Figure 2.12 Graph showing the dehydration curve (green) and DSC curve (blue) of material #1 via TGA analysis. Source: Created by the Author.

The thermogravimetric analysis (TGA) was performed on material #3 to evaluate roughly the occupancy and role of H_2O as an extra-framework component. There are two dehydration events seen in Figure 2.12 shown by both the TGA and DSC curves. Overall, there is about 11% of water loss in the structure. The XRD analysis of the dehydrated material (Figure 2.13) showed no distortion of its pattern from the original material.

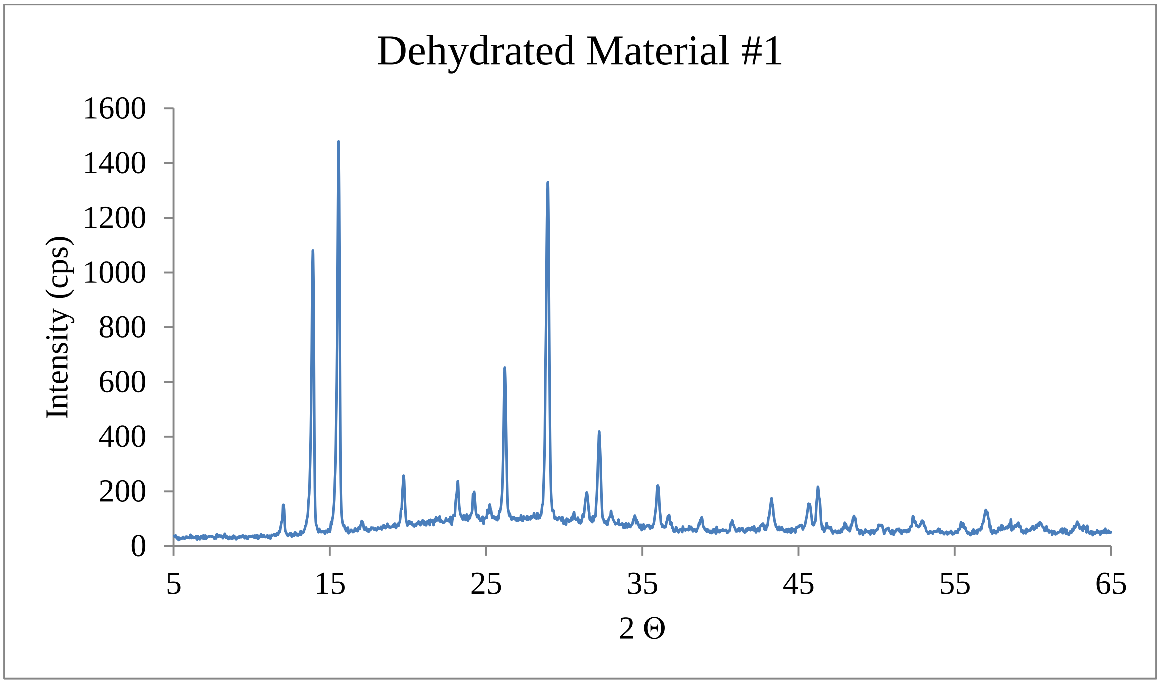

Fig 2.13 Graph showing the XRD pattern of the dehydrated material #1. Source: Created by the Author.

Discussion

Material #1 was exchanged with H^+, K^+, Cs^+ and the K^+-form was back exchanged with Na^+. The four of these exchanges were analyzed with Raman microscopy, which illustrated that there was a large amount of shift in the v5 peak that signifies the 3MR geometry. Material #1 readily accepted the cations into its structure with rates decreasing as follows: material #3, material #4, material #5, material #6. Protonation occurred more rapidly, followed by K^+ exchange, then Na^+ back exchange, and Cs^+ was the slowest. The trend makes sense, since the smaller the ion, the more easily it can pass through the channel pathways and interact with the framework. With the case of Na^+ back exchanging, it shows that there is some preference to Na^+ over K^+ though it does take more time to push the K^+ out of the structure. Na^+ is also unable fully occupy all 24 of the sites, leaving room for some K^+ ions.

Material #3 and material #4 exhibited a shift to higher wave numbers. The 3MR in this case is straining the Si-O1 and Si-O2 bonds, causing a lengthening of the Si-O3 bonds, which then opens the ring to allow for the new larger ion to interact with the framework. Material #5 shows a trend towards a lower wave number in an attempt to restore the material structure to its original state; however, in material #6, in response to the Cs^+ uptake, the shift is to lower wave numbers suggesting a stretching of the Si-O bonds in the SiO_4 of the 3MR, thereby also leading to an increased size in the unit-cell and the 7MR to accommodate the large Cs^+ ion.

Material #3 and material #4 were evaluated in situ using synchrotron X-ray diffraction in order to understand any structural changes through time. In both cases the unit-cell increased in length. Material #3 had a straining of the 3MR yielding a lengthening in the SiO_4 tetrahedra forcing the ring structure to open (as seen by the 3MR dihedral and Si-O bond lengths). The impacts of this are discussed further in Chapter 4. Material #4 did not exhibit as much of a cell increase as material #3, but some was likely due to the increase in size between the host Na^+ ion and the in-going K^+ ion, a difference of 0.36 Å (Shannon and Prewitt 1969).

The structure material #3 was refined to have the formula $H_{1.3}Na_{0.7}ZrSi_3O_9 \cdot 3H_2O$, though there is some positional disorder likely among the Na^+ and H_2O sites, full protonation and removal of Na^+ cannot occur. Material #4 was found to be $K_2ZrSi_3O_9 \cdot 1H_2O$, though the K^+ occupancy is in disorder with both Na and H_2O, and is likely less concentrated than the formula suggests. The Na^+ and K^+ sites are very close; however, the average bond distance to framework O increase from Na-O to K-O (2.59Å and 2.73Å, respectively). The dihedral angle also resulted from the sequential Rietveld refinements and in material #4 changed from 5.4º to 4.6º. This is not a significant amount of change in the 3MR.

TGA showed that material #1 possessed 11 weight percent H_2O, which was removed from the structure in a two-step process. The first step shown in both TGA and DSC, Figure 2.12, is likely due to the loss of any adsorbed water, the sec step is the more coordinated waters in the pathways. The XRD analysis showed that there was minimal alteration to the structure as a whole due to dehydration. The 11% H_2O loss is in agreement with previous studies done on the materials original synthesis (proprietary). Both the Raman and XRD data show that the 3MR plays a large role in the ion exchange mechanism for material #1; this is where there is the greatest amount of distortion to allow for exchange to occur. The data are also in agreement for the time frame in which these exchanges occur. The protonation also really causes the cage structure to open up, which is be discussed in Chapter 4.

Conclusion

Material #1 was exchanged with H^+, Na^+, K^+, and Cs^+ in this study to understand the ion exchange process and mechanisms involved during ion exchange that enable the structure to have an affinity towards K^+ over the other monovalent cations, as well as a reason for the rejection of multivalent ions. The structural control on ion exchange in this material is the 3MR that acts to manipulate the larger 7MR and 6MR structures.

Despite the size constraints, the large Cs^+ ion was able to enter the structure slowly and resulted in great distortion of the structure, residing within the cage structure. It is also evident that the K^+ and Na^+ sites are nearly identical, which results in disorder among the ions when both are present. There is some affinity towards Na^+ as it was able to take the place of K^+ when back exchanged.

Chapter 3

Ion Exchange processes in ~$HNaZrSi_3O_9$ • $2.8H_2O$ – Material #2

Introduction

Material #2 is the partially protonated form of material #1 generated by the Source Company. Material #2 was found in in-vitro studies to more rapidly sequester K^+ into its structure than the material #1, Na^+ form (Anker et al. 2013; Kosiborod et al. 2014; Packham et al. 2014; Rafique et al. 2015). The ion selectivity mechanism for this process was previously thought to be a removal of the hydration shell around the host channel cation and that the K^+ would be in a 4-fold coordination with the framework instead of 2-fold with Na^+ resulting in a stronger affinity for K^+ (Stavros et al. 2014). Protonation of the material was found to shorten the ZrO_6 bonds, which causes the channels to open up and more effectively, and allow for coordinated hydration to occur.

Material #2 was exchanged with Na^+, K^+, and Cs^+ to evaluate the mechanism behind the selective affinity towards the K^+ ion. This study found that protonation inhibited the larger cation, Cs^+, from entering the structure, as well as enhanced the uptake of the smaller monovalent cations. The protonation is also likely responsible for the prevention of multivalent cations that are too positively charged to enter the structure.

Methodology

Ion Exchange

The ion exchange was done via a flow through cell as discussed in Chapter 2. The flow rate of the exchanging solution will be held constant at a rate of 0.05 mL/min for the entirety of each experiment by means of a peristaltic pump (e.g., Celestian et al. 2013). The sapphire cell used for these experiments is discussed fully in Chapter 2

(Figure 2.1). The conditions Table 3.1 below shows the exchanges studied with material #2 and resulting material.

Table 3.1. The resultant materials of ion exchange in the experiment.

Original Material	**Ion Exchange**	**Resulting Material**
#2	Na^+	#7
	K^+	#8
	Cs^+	#9

Source: Created by the Author.

Sodium

To evaluate any preference to Na^+ over K^+, a 0.1 M solution was made by adding 5.8 g of NaCl (s), 99^+ % purity, to 1 L of deionized H_2O. The increased concentration would increase the Donnan potential in order to try to force exchange to occur.

Potassium

Material #2 is a partially protonated form of material #1 and it is thought to also be highly selective of K^+ ions. In order to verify this and to understand the structural changes that occur as K^+ ion exchange takes place, the ion exchange was completed by flowing a 0.01 M solution of KCl through the cell. The solution was made by adding 0.74 g of KCl (s), 99^+ % purity, to 1 L of deionized H_2O.

Cesium

The Cs^+ ion is larger than K^+ by 0.29 Å. The goal of ion exchanging material #2 with Cs^+ was to identify the changes in the crystal structure to accommodate the large cation and the rate at which this occurs. The Cs^+ would have to distort the structure in order to pass through the ion channels. The solution was made to be 0.01 M, equating to 1.68g of CsCl (s), 99.99 % purity, to 1 L of deionized H_2O.

Raman Spectroscopy

The time-resolved Raman studies were performed using a DXR Raman Microscope with a 780 nm near infrared laser. The analysis was set to 10 sec exposures three times for a total of a 30-sec scan, or frame. There was a total of 400 frames, which yields approximately a 3.3 hour timespan over which data were collected to track the changes in the Raman spectrum through time. More details can be found in the methodology section of Chapter 2.

X-ray Diffraction

The time-resolved X-ray synchrotron diffraction (XSD) studies were performed at the Advanced Photon Source at Argonne National Laboratory in Illinois. The synchrotron data provided the high flux source needed to rapidly collect data necessary for time-resolved studies. The XSD studies were carried out using a similar cell design as the sapphire cell (Figure 2.1), but it was made of polyamide tubing rather than sapphire. Polyamide weakly scatters and, therefore, is more desirable in XSD studies. A more detailed description of XSD and data processing can found in the methodology of Chapter 2.

Thermogravimetric Analysis

H_2O is a significant constituent of the thesis materials and is necessary to understand the mechanism for ion exchange. The mechanism for ion exchange was thought to be a hydration effect due to the hydration shell of the extra-framework ions. To evaluate the role of water and of the protonation of the material, material #2 was analyzed with a Netzsch STA 449 F1 Jupiter with TGA and DSC analyzers. Approximately 10 mg of the material was heated to 600 ºC at 1 ºC/min in air. The analysis would determine the weight loss due to a loss of water. After the TGA analysis, material #2 was analyzed via a Rigaku MiniFlexII Desktop Powder X-ray diffractometer to evaluate any major structural changes.

Results

Raman Studies

Material #2 is the partially protonated form of the research material. Material #2, like material #1, was kindly provided by the Sponsor Company to evaluate any affinity to the K^+ ion. Raman microscopy was used to analyze material #2 (Figure 3.1) prior to exchange with Na, K, and Cs (Figures 3.2, 3.3, and 3.4, respectively). Similar to what was observed in material #1, the v5 peak at 520 cm^{-1} was found to exhibit the greatest amount of shift during ion exchange in all cases, and its position relates to the distortion of the 3MR (the 3MR are the building blocks of the 7MR channels). The 417 cm^{-1} and 645 cm^{-1} peaks are representative of the sapphire cell used to calibrate the laser during the experiment to ensure that observed trends are in fact a result of structural distortion, not temperature fluctuation of the laser. The 900 cm^{-1} to 1000 cm^{-1} range is due to the Si-O bonds, where the v5 peak is representative of straining of dihedral angle in the 3MR of the thesis material (Figure 3.1). Figures 3.2 to 3.4 show the Raman shift of the v5 peak during their respective exchanges.

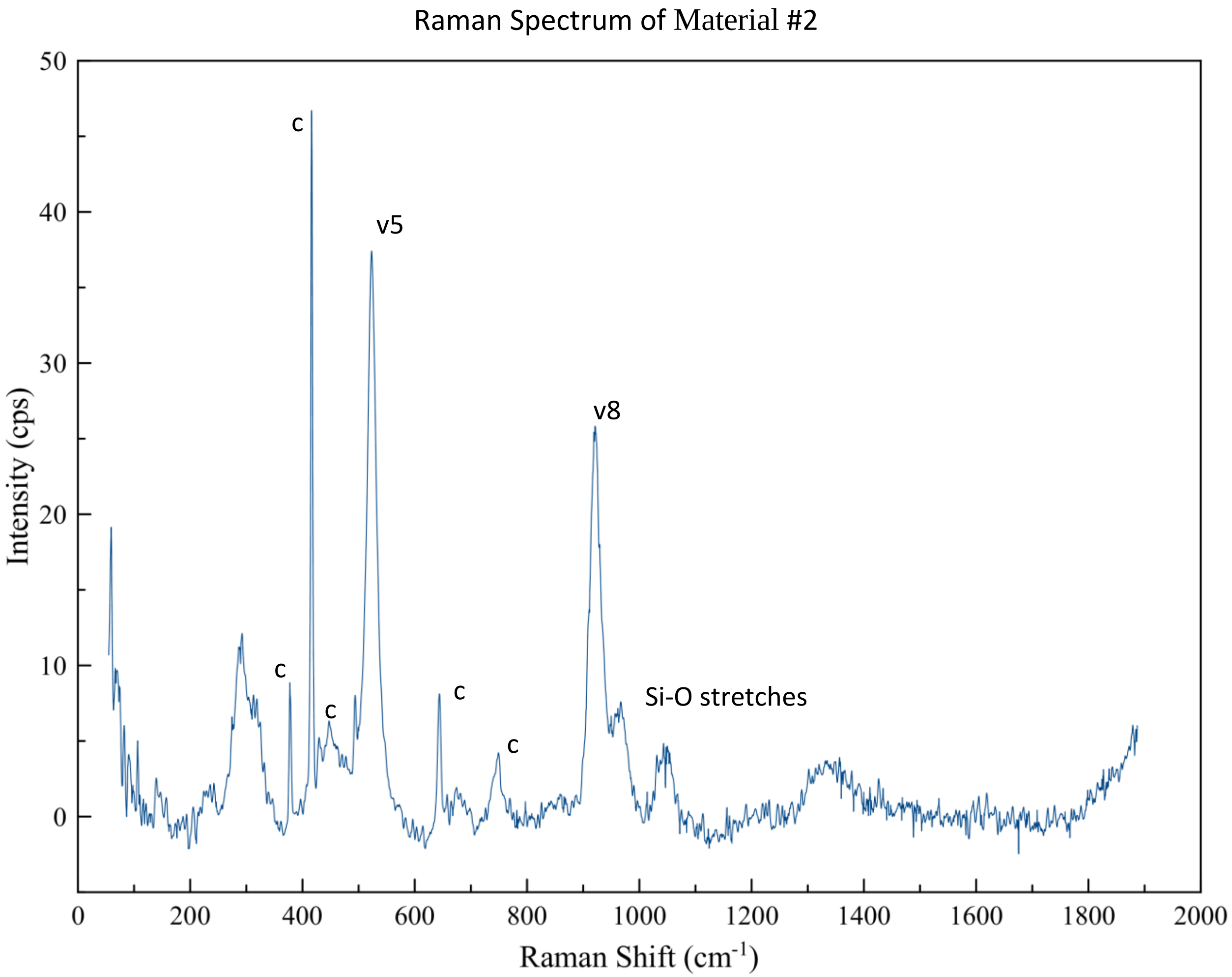

Figure 3.1 The Raman spectra for material #2, the partially protonated form of material #1, where “c” refers to sapphire peaks. Source: Created by the Author.

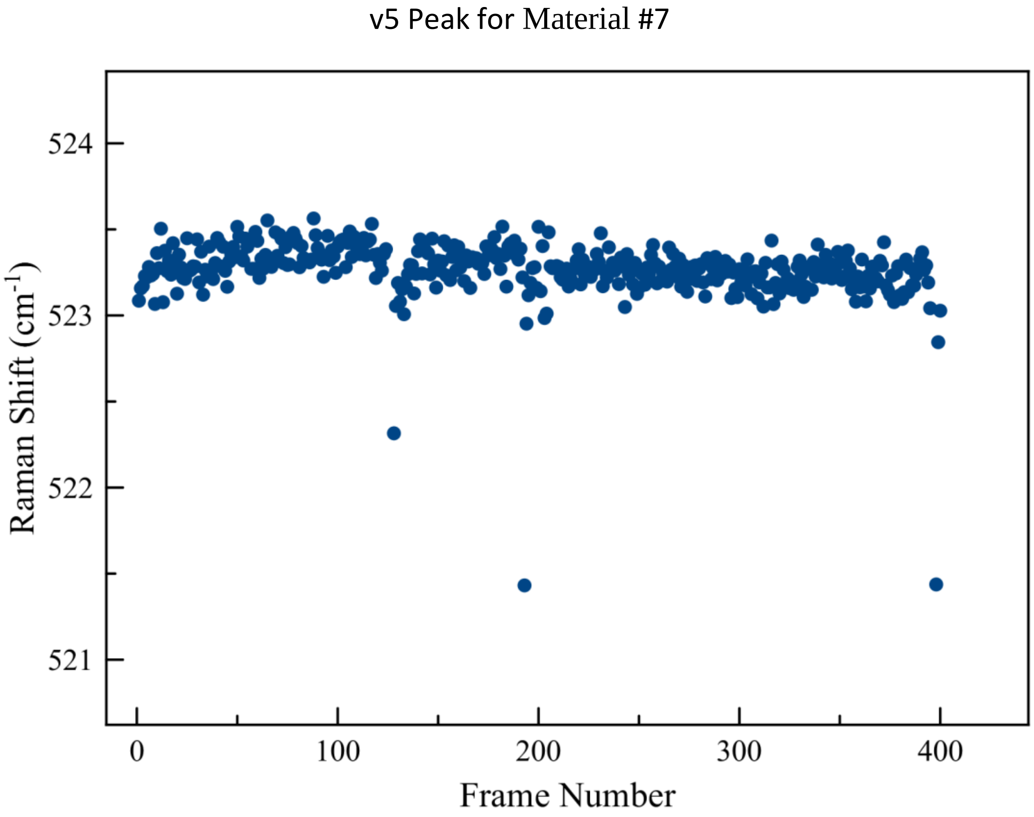

Figure 3.2 Graph showing the change in the v5 peak, which would signify distortion of the 3MR, of the Na^+ exchange into material #2. Here, no changes in the v5 peak position were observed during Na exchange; therefore, it is likely that Na exchange did not occur. Source: Created by the Author.

Figure 3.2 shows the time-resolved Raman signal for changes in the v5 peak of material #7. Material #7 is the Na^+ exchanged form of material #2, which attempts to return the material back to material #1. As seen above, the v5 peak does not respond to the Na^+ solution passing through it. The Na^+ is unable to exchange and push the H^+ protons out of the structure. The trend in the v5 is effectively a 0 cm^{-1}/frame number slope over the 400 frames.

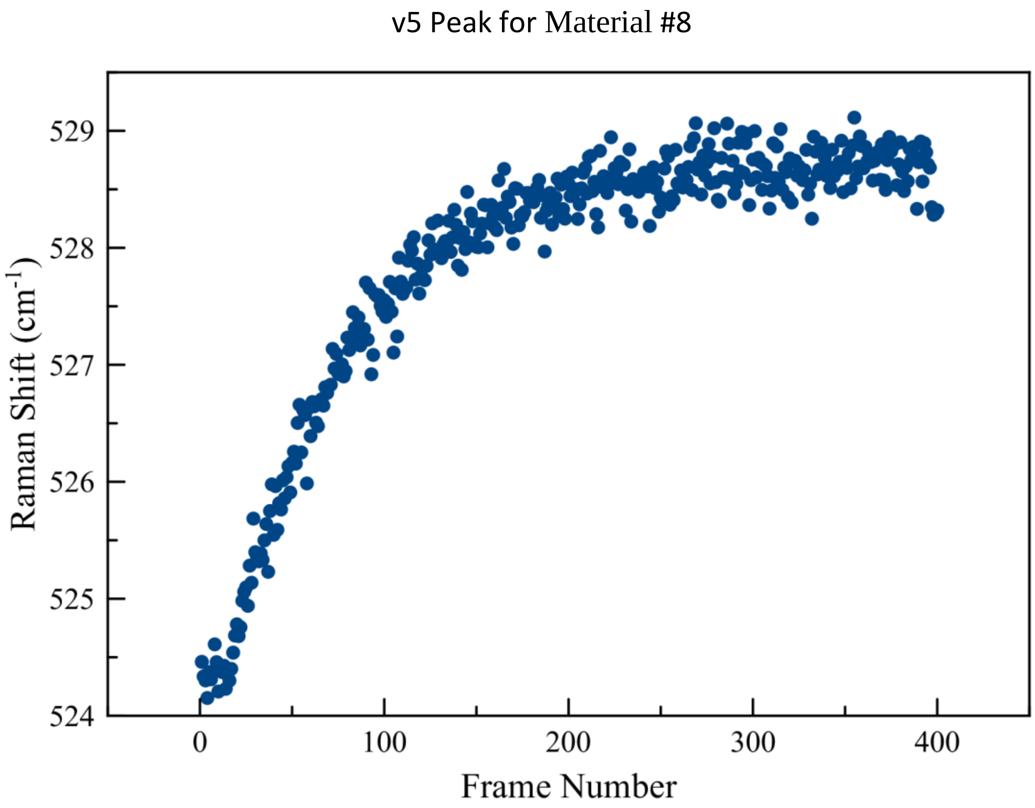

Figure 3.3 Graph showing the change in the v5 peak, which signifies distortion of the 3MR, of the K$^+$ exchange into material #2. Source: Created by the Author.

Figure 3.3 shows the time-resolved Raman data for the v5 peak in the material #8 material. Material #8 is the K$^+$ form of material #2. As the K$^+$ ions move into the crystal structure there is a shift to higher wave numbers in the 3MR peak. The exchange of K$^+$ into material #2 occurs nearly from frame 0 and stops changing near frame 325. Exchange in this experiment reaches completion and therefore maximum amount of exchange after 3.2 hours of exposure to the 0.01M KCl solution. Over the duration of the experiment the v5 peak shifts from 524.2 to 528.6 cm^{-1} for a total of 6.4 cm^{-1}. The positive shift suggests a shortening in the Zr-OH bonds.

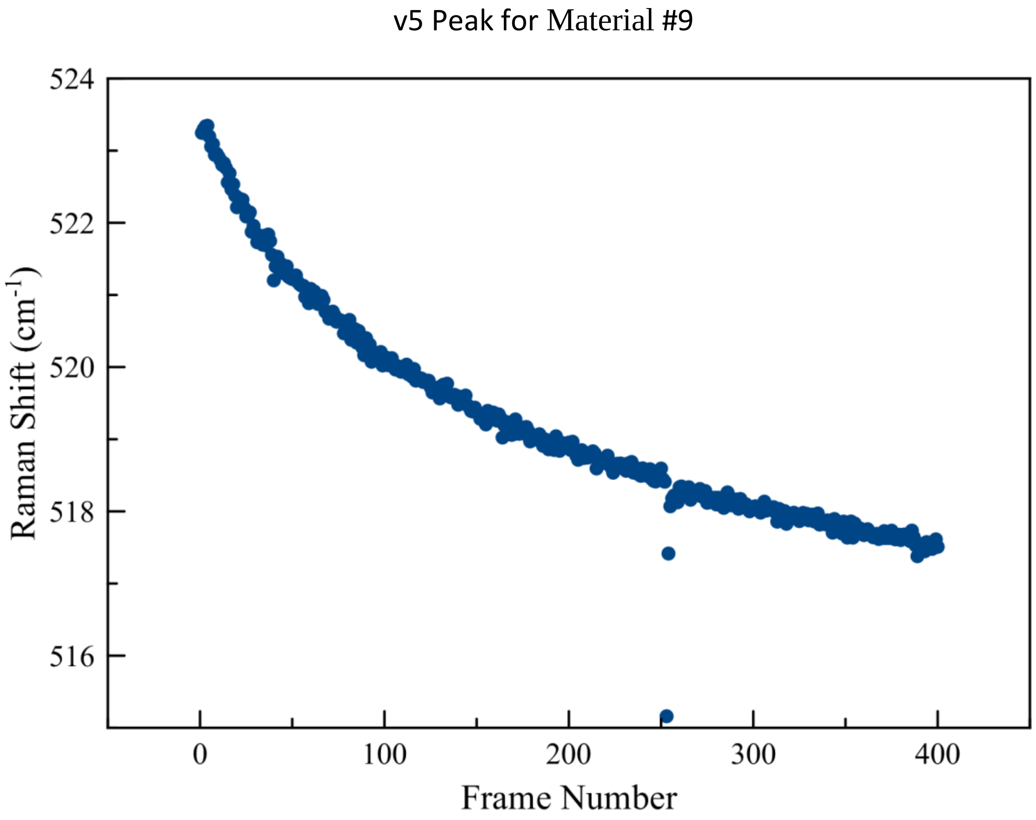

Figure 3.4 Graph showing the change in the v5 peak, which signifies distortion of the 3MR, of the Cs$^+$ exchange into material #2. Source: Created by the Author.

Figure 3.4 shows the trend of the Cs$^+$ exchange into material #2 yielding material #9. As Cs$^+$ enters the channel pathways and enters into the crystal structure it causes the 3MR geometry to shift towards lower wave numbers. The v5 peak shifts from 523.4 cm^{-1} to 517.4 cm^{-1}; therefore, a total 6 cm^{-1} shift over the 400 frames. The overall negative trend signifies a lengthening of the Zr-OH bonds. The trend suggests that it would continue on and level off shortly after frame 400 to reach maximum exchange.

XSD Studies

The XSD studies are time-resolved experiments performed at the APS Synchrotron Source and the initial structure of material #2 (Figure 3.5) was provided by the Sponsor Company. Due to time constraints and beam time limitations, not all of the Raman experiments were recreated at the APS. The exchanges performed with material #2 were K^+ and Cs^+ (material #8 and material #9, respectively).

Material #2 has an increased amount of H^+ compared to material #1. Similar to material #1, the H_2O sites are disordered with the monovalent extra-framework cation. The disordered H_2O sites are farther away from the cage center toward the cage walls in the material #2 material. The 3MR torsion angle for the material #2 material is 6º, a 0.6º increase from material #1. The change in the dihedral angle is insignificant.

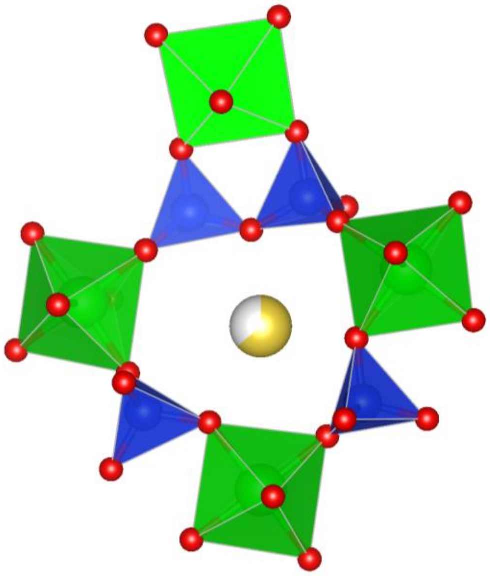

Figure 3.5 A model of the structure of material #2, with the Na^+ site in the center of the 7MR, denoted by the partially filled yellow sphere. Source: Created by the Author.

The Na^+ site in material #2 remains in the center of the 7MR seen in Figure 3.5. The average Na-O bond in material #2 is 2.61Å. The unit-cell of material #2 is 12.780 (2) Å along the a- axis, therefore 2087.337 (7) $Å^3$ in volume. The unit-cell is larger than that of material #1 at 12.740 (1) Å along the “a” axis, with a volume of 2067.800 (5) $Å^3$.

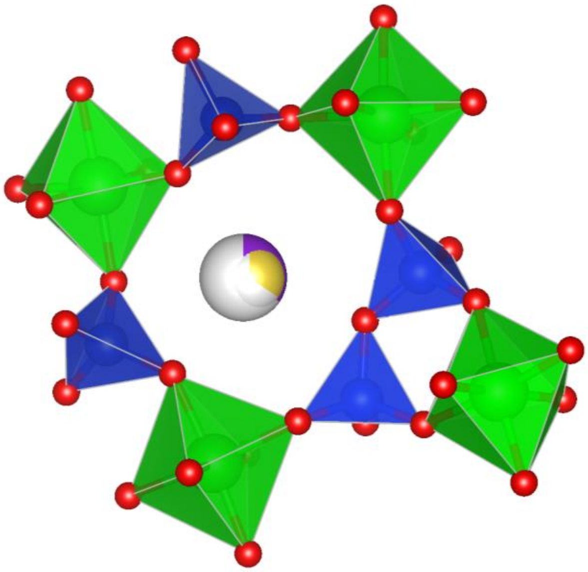

Figure 3.6 A model of **t**he structure of material #8, with the Na^+ site in the center of the 7MR, denoted by the partially filled yellow sphere, which is in disorder with K^+ site at the same location. Source: Created by the Author.

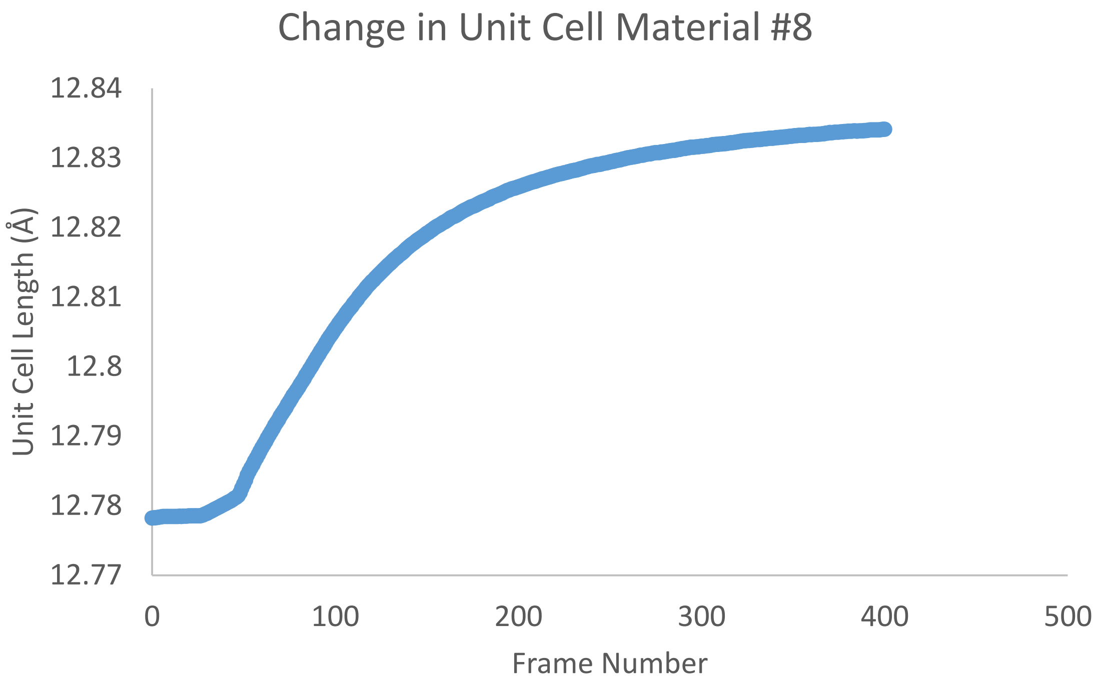

Figure 3.7 Graph showing the changes in the unit-cell of material #8 through time resulting from K^+ exchange of material #2. The plot is comprised of individual points and is not a trend-line. Source: Created by the Author.

The XSD results of the K^+ ion exchange into material #2 indicate that there is an increase in the size of the unit-cell of the material seen in Figures 3.6 and 3.7. Figure 3.6 shows a representation of the structure after it has been maximally exchanged with K^+. The increase is to be expected as K^+ has a larger ionic radius. As seen in Figure 3.7 the unit-cell increases 0.55 (1) Å in length along a given axis. The XSD data illustrated that the K^+ ion resides in almost the exact same site as the Na^+ ion. Both of the monovalent cations can be found in the structure (i.e. positional disorder), even at maximum exchange. The sites are disordered with one another with a 33% chance of Na^+ and 67% chance of K^+ occupying the extra-framework cite. H_2O was evaluated and represented as O ions (Ow in the structure label codes, because H does not appreciably contribute to the phase shift of the scattered diffraction vector), which are not represented in Figure 3.6, and also occupy sites that surround the monovalent cations and are also in coordination with the framework. On either side of the cations there is an Ow site in the channel. The average measured bond-lengths for Na-O and K-O increased from material #2 to material #8 as expected (2.61 Å and 2.7 Å, respectively). The increase in the unit-cell agrees with the necessary increase in size to accommodate the larger K^+ ion and its hydration shell.

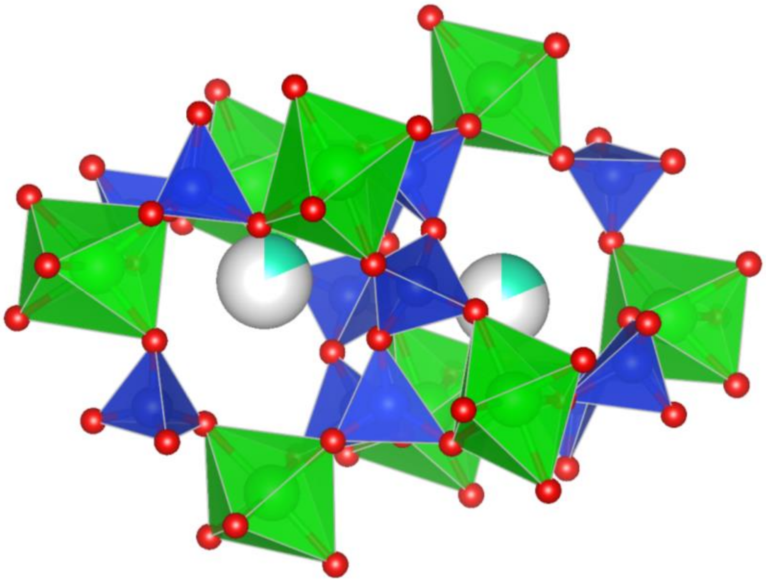

Figure 3.8 A model of the structure of material #9, with the Cs^+ site off to the side of the 7MR located more towards the center of the cage structure denoted by the partially filled light blue spheres. H_2O is not shown for clarity. Source: Created by the Author.

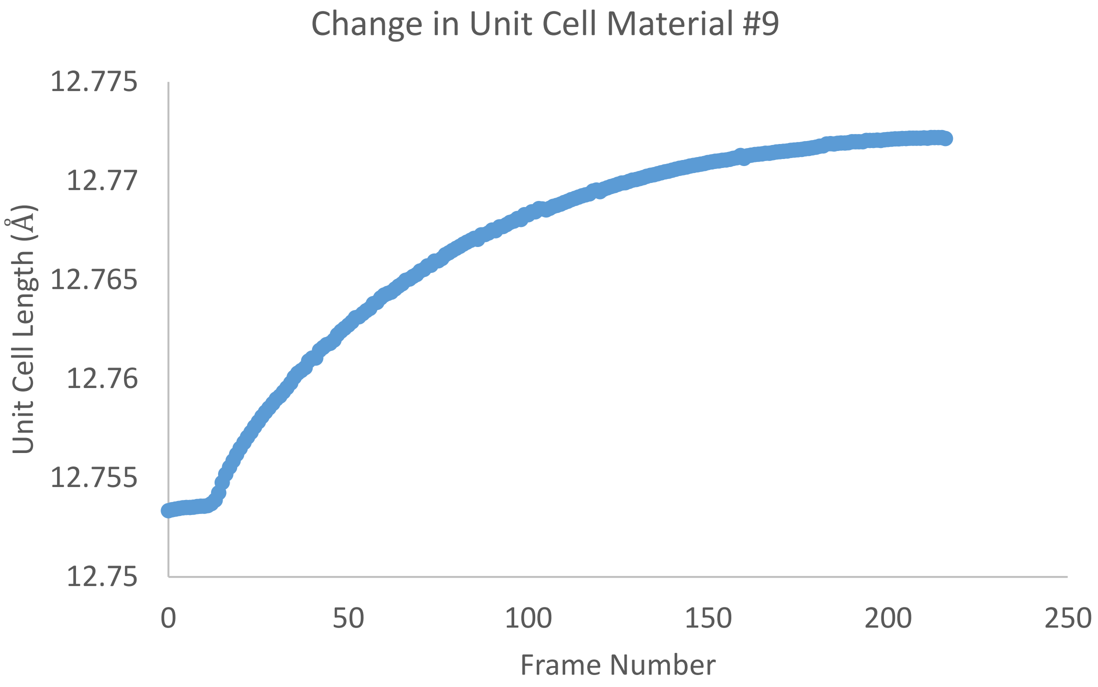

Figure 3.9 Graph of the changes of the unit cell size during ion exchange forming material #9. The plot is comprised of individual points and is not a trend-line. Source: Created by the Author.

The XSD study performed on Cs^+ exchange into material #2 revealed that some amount of exchange does occur and results in a distortion and slight increase in the size of the unit-cell (Figures 3.8 and 3.9). Given more time, the exchange would likely continue the trend of increasing unit-cell size. Due to time constraints at APS, a longer exchange could not be completed.

In Figure 3.8, the Cs^+ ion is located inside the cage structure, unlike the other monovalent ions in this study. The 7MR is not large enough to accommodate the Cs^+ ion and its hydration shell.

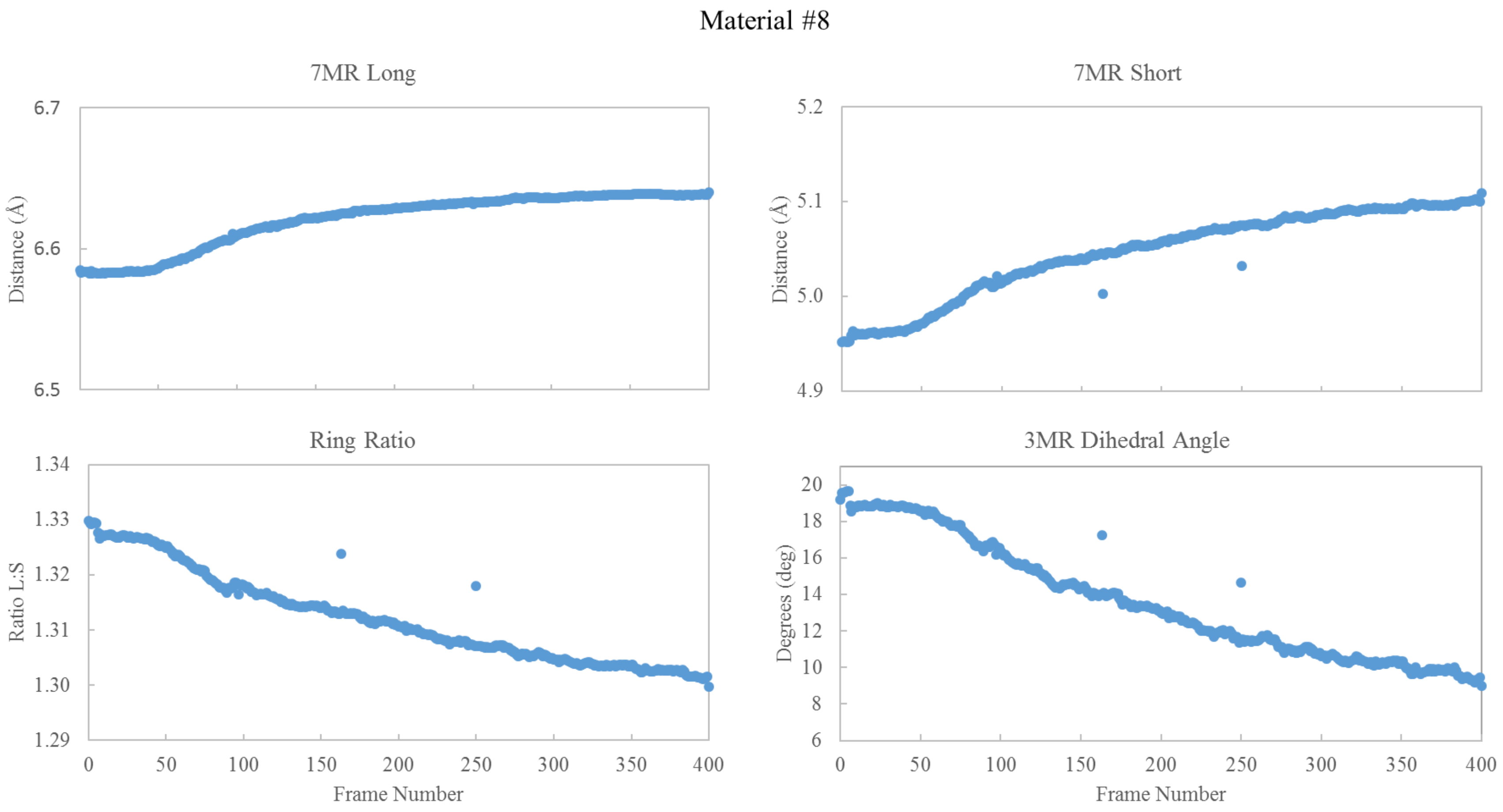

Figure 3.10 Plots represent the changes in O…O distances; O1…O3 (upper left), O2…O3 (upper right), ratio of the O1…O3 and O2…O3 (lower left) and the changes in the dihedral angle of the 3MR (lower right) in the material #8 sequential synchrotron data. Source: Created by the Author.

In the resulting K^+ exchanged material #2 (material #8), the long and short both show an upward increasing trend (Figure 3.10); however, the ratio between the long and short O...O suggests that the increase in the short O2…O3 is increasing faster than the O1…O3. The O2…O3 increases 1.5 Å over the full exchange, while the O1…O3 increases 0.03 Å. The distortion index along the Zr-O2-Si-O3 dihedral angle within the 3MR substructure shows a negative trend as time progresses with an overall 10º change.

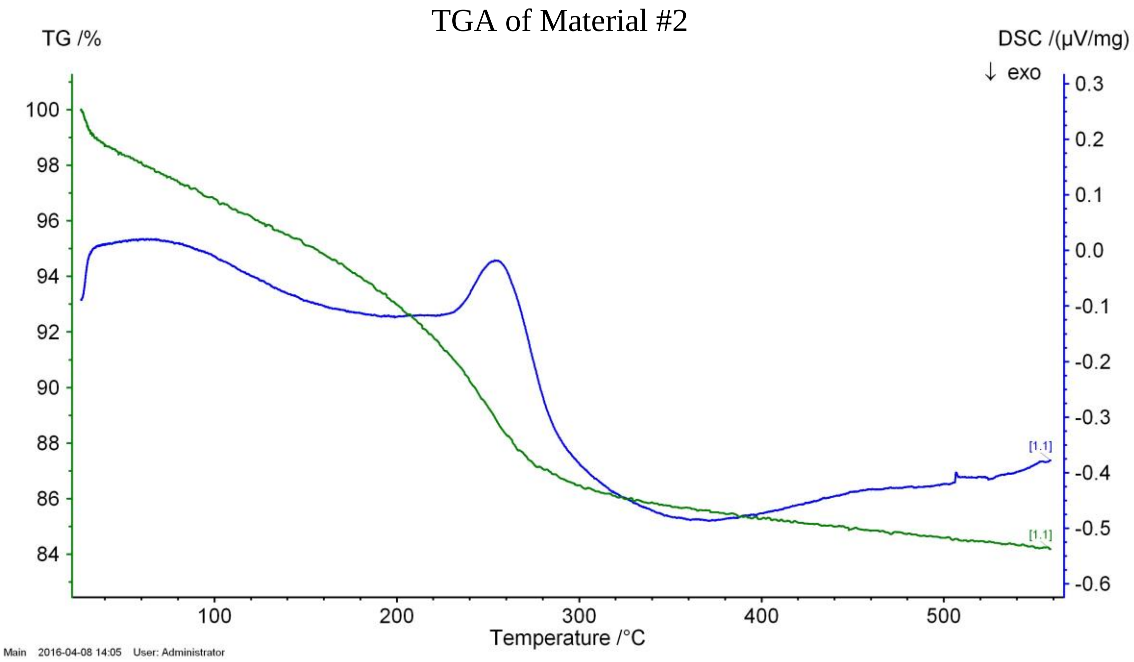

Figure 3.11 Graph showing the dehydration curve (green) and DSC curve (blue) of material #2 via TGA analysis. Source: Created by the Author.

TGA Study

The TGA was performed on the material #2 to evaluate roughly the occupancy and role of water as an extra-framework component. There is one major dehydration event seen in Figure 3.11 above from 240 to 300 ºC. Overall there is about 16% of a H_2O loss in the structure. The XRD analysis of the dehydrated material showed distortion, and the material's XRD pattern weakened, moving towards a more amorphous material (Figure 3.12).

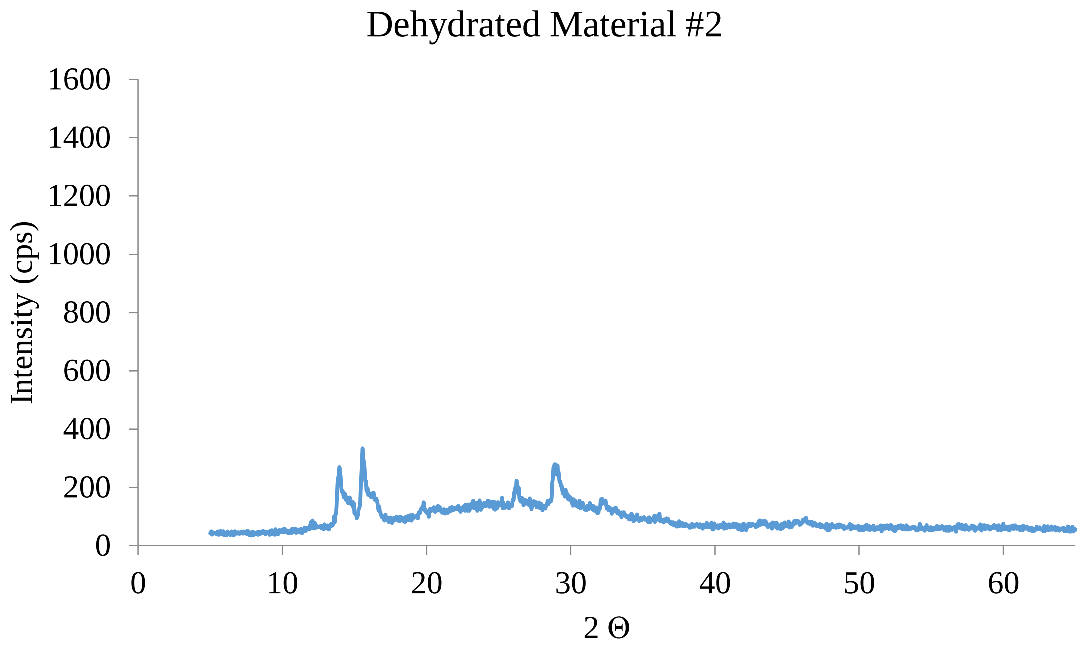

Figure 3.12 Graph showing the XRD pattern of the dehydrated material #2.
Source: Created by the Author.

Discussion

The time-resolved Raman studies showed that under the conditions tested there was decreased affinity to Na^+ (Figure 3.2), and this suggests that, due to the increased presence of H^+ in the structure, Na^+ is unable to exchange. Na^+ does not possess the proper size or ionic potential to overcome the repulsive forces of the framework protons.

The K^+ ion exchange, as seen in Figure 3.3, and the structural information in Figure 3.6 show that the K^+ is able to overcome the protonation effects and enter the structure. Material #2 is not maximally protonated, so there is still Na^+ in the structure. As noted, the K^+ moves to similar site as the Na^+ ion causing disorder among them and the coordinated waters.

Cs^+ is able to exchange into the partially protonated material, but shows a negative trend in the Raman shift, the opposite of K^+ (Fig 3.4). The unit-cell of both these exchanges increase, Figures 3.7 and 3.9 (K^+ and Cs^+, respectively). The v5 peak responds differently in each case of K^+ or Cs^+ exchange. Cs^+ would have to cause a great deal of 3MR distortion to be accommodated, which is likely responsible for the negative trend in the Raman shift. Cs^+ does not reside in the same site as K^+ and Na^+, its large size requires longer bond distances and therefore is forced to more towards the center of the cage structure (Figure 3.8).

Conclusion

Material #2 is the partially protonated form of material #1. Material #2 was exchanged with Na^+, K^+, and Cs^+ in this study to understand the ion exchange process and mechanisms involved during ion exchange that enable the structure to have an affinity towards K^+ over the other monovalent cations. The control on ion exchange in the material is the proton (as OH) acting as a lever. The proton must be moved to accommodate the new extra-framework cation.

Despite the size constraints, the large Cs^+ ion was able to enter the structure slowly, resulting in great distortion of the structure, and forcing the Cs^+ to ultimate reside within the cages. It is also evident that the K^+ and Na^+ sites are nearly identically positioned, and results in disorder among the ions when both are present. There is no affinity to Na^+ in the partially protonated material; however, the larger K^+ and Cs^+ ions were able to exchange in the Na^+ sites suggesting greater affinity.

Chapter 4

Ion Exchange Processes in $H_{1.3}Na_{0.7}ZrSi_3O_9 \cdot 3H_2O$ – Material #3

Introduction

Material #3 is the maximally protonated form of the thesis material generated by the author. The material was tested to evaluate the role of H^+ when the host extra-framework cations are nearly entirely removed from the material. The H^+ are thought to protrude into the 7MR rings at the bridging O^{2-} of Zr-O-Si. Neutron scattering would be needed to verify this position, but the response of the structure during exchange and Valence Bond Theories suggests that this location is likely correct. The position of the H set up an ordered H_2O bond network in the center of the channels, causing the structure to open to allow for further hydration and larger channel space. The positive charge (and the strong polar covalent bond of the OH) of the protons also acts as a barrier preventing large ions, highly charged ions, or ions that are too small from interacting with the framework. The K ion fits into the ring structure easily in the protonated form, and the hydration energy of K is such to overcome the OH...H_2O repulsive forces.

The exchange processes of the materials were analyzed with in situ time-resolved Raman microscopy and XSD to identify any structural changes or deformations during the exchange of Na^+, K^+, and Cs^+ ions.

Methodology

Ion Exchange

The ion exchange was carried out via a flow-through cell by means of a peristaltic pump, so that the material would be exposed to a constantly refreshed solution to minimize any effects of local exchange equilibriums. The flow rate was set to 0.05

mL/min. The sapphire cell seen in Figure 2.1 was utilized for the time-resolved Raman studies of material #3 ion exchanges.

Table 4.1. The resultant materials of ion exchange in the study.

Original Material	Ion Exchange	Resulting Material
#3	Na^+	#10
	K^+	#11
	Cs^+	#12

Source: Created by the Author.

Sodium

To evaluate any preference to Na, a 0.1 M solution was made by adding 5.8 g of NaCl (s), 99^+ % purity, to 1 L of deionized H_2O. The increased concentration of Na^+ would attempt to force ion exchange to occur; if no exchange occurred, then the material would have very weak affinity to the host Na^+ ion.

Potassium

In order to verify the affinity for K^+ and to understand the structural changes that occur as K^+ ion exchange takes place, the ion exchange of K^+ was completed by flowing a 0.01 M solution of KCl through the cell. The solution was made by adding 0.74 g of KCl (s), 99^+ % purity, to 1 L of deionized H_2O.

Cesium

Cs is the largest stable ion of on the periodic table. The goal of ion exchanging material #3 with Cs^+ was to identify if the structure would distort in order to accommodate large size of Cs^+ as well as see if the protonation would allow for the large ion to enter the extra-framework sites. The solution was made to be 0.01 M, which equates to 1.68 g of CsCl (s), 99.99 % purity, to 1 L of deionized H_2O.

Raman Spectroscopy

Data from time-resolved Raman spectroscopy studies were used to model the molecular distortions and changes taking place to the bonds within the material during ion exchange, for which Raman is an ideal tool (see Chapter 1). Changes in the Raman shift generated by the structural changes will be measured and analyzed (e.g., Celestian et al. 2013), and atomic structural models derived from this study will help reveal exchange pathways of in-going cations. The Raman spectra were fit using MagicPlotPro to evaluate the peak position changes and kinetics of ion exchange. The time-resolved Raman studies were performed using a DXR Raman Microscope with a 780 nm near infrared laser. For detailed parameters for the Raman Microscopy, see Chapter 2.

X-ray Diffraction

X-ray diffraction is also required to better evaluate the crystal structure during the ion exchange process. In order to have time-resolved XRD data, a high flux source is necessary to generate the X-rays rapidly; therefore, synchrotron radiation was used to obtain the required high flux of X-rays for rapid data collection (Celestian et al. 2013). Structural models were developed using the Rietveld refinement implemented in the GSAS-II software (Toby and Von Dreele 2013).

The time-resolved XSD studies were performed at the Advanced Photon Source at Argonne National Laboratory. The XSD studies were carried out using a cell made of polyamide tubing instead of the sapphire cell used in the Raman studies. Polyamide weakly scatters (unlike sapphire) and, therefore, is desirable for XSD studies. A detailed description of the parameters of the XSD experiments can be found in Chapter 2.

Thermogravimetric Analysis

H_2O is a significant constituent of the research materials and especially in material #3. The unit-cell of material #3 is larger than material #1 and material #2 and is kept open by the presence of H_2O bond network. To evaluate the extent of hydration and of the thermal stability of the maximal protonated material, material #3 was analyzed with a Netzsch STA 449 F1 Jupiter with TGA and DSC analyzers. Approximately 10 mg of the material was heated to 600 ºC at 1 ºC/min in air. The analysis illustrated weight loss due to H_2O evaporation. After the TGA analysis of material #3 was analyzed via a Rigaku MiniFlexII Desktop Powder X-ray diffractometer to evaluate any major structural changes within the material.

Results

Raman Studies

Material #3 is the maximally protonated form of the thesis material. Material #3 was generated via H^+ exchange of material #1 as discussed in Chapter 2. The role of material #3 was to evaluate the influences of protonation on the ion exchange and selectivity processes. Raman microscopy was used to analyze material #3 (Figure 4.1) prior to exchange with Na^+, K^+, and Cs^+ (Figures 3.2, 3.3, and 3.4, respectively). Similar to what was observed in the material #1, and material #2 materials, the v5 peak at 520 cm^{-1} was found to exhibit the greatest amount of shift during ion exchange in all cases. The 417 cm^{-1} and 645 cm^{-1} peaks are representative of the sapphire cell used to calibrate the laser during the experiment to ensure that observed trends are in fact real. The 900 cm^{-1} to 1000 cm^{-1} range is due to the Si-O symmetric and asymmetric stretches, where the v5 peak is representative of distortion of the dihedral in the 3MR of the thesis

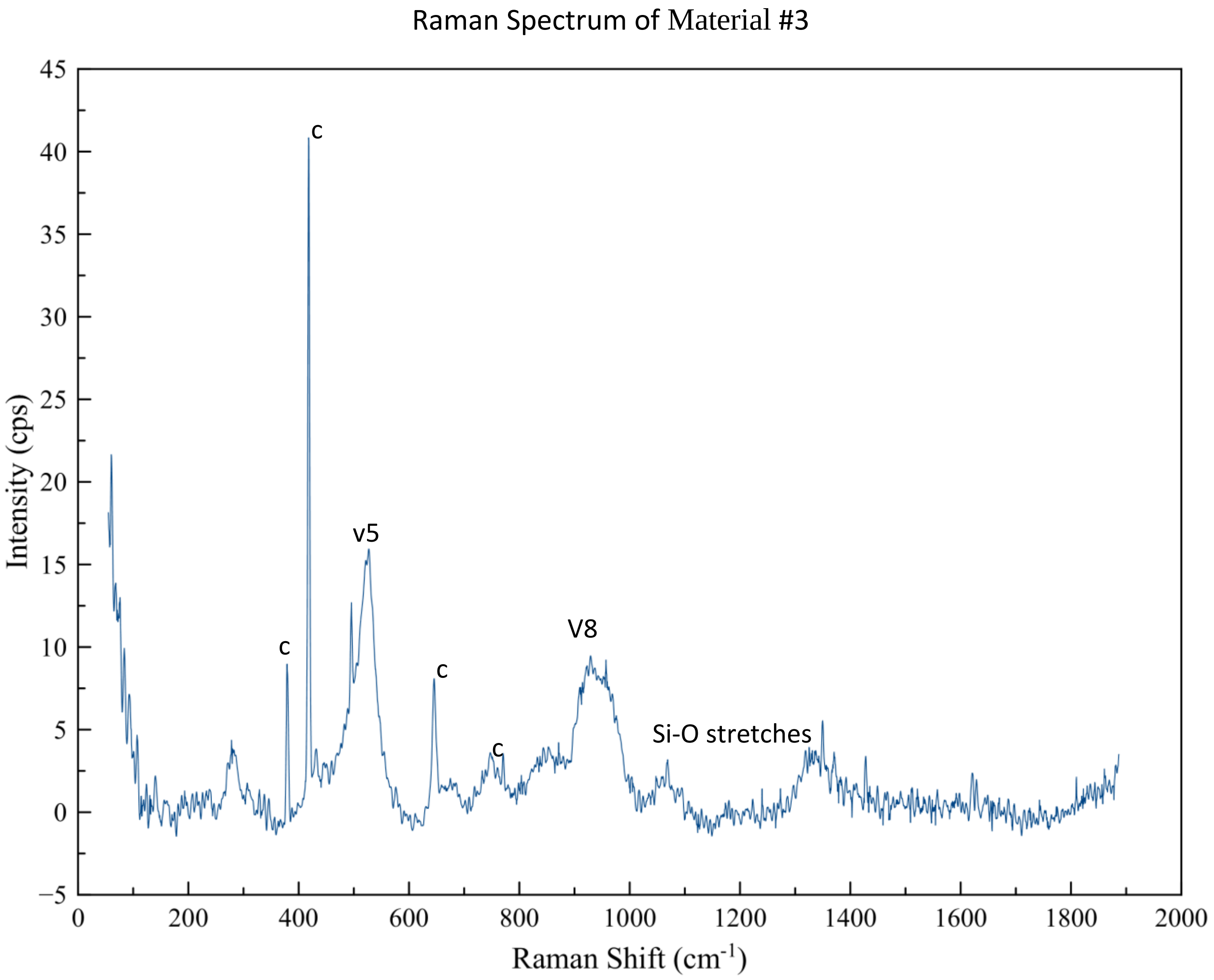

Figure 4.1 Graphing showing the Raman spectra for the material #3, the maximally protonated form of material #1, where "c" refers to sapphire peaks. Source: Created by the Author.

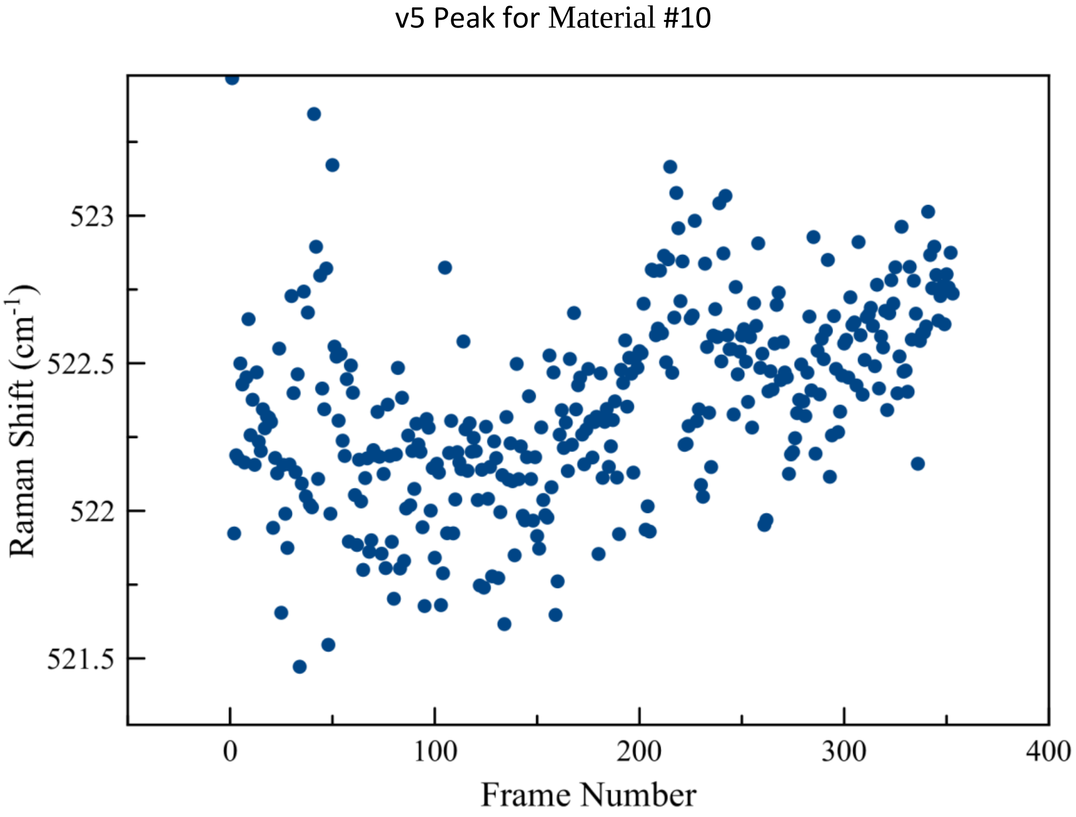

Figure 4.2 Graph showing the change in the v5 peak, which signifies distortion of the 3MR, of the Na^+ exchange into material #3. Source: Created by the Author.

material (Figure 3.1). Figures 4.2 to 4.5 show the Raman shift of the v5 peak during their respective exchanges.

Figure 4.2 shows the time-resolved Raman signal for changes in the v5 peak of material #10. Material #10 is the Na^+ exchanged form of material #3, which was utilized to evaluate a preference to the Na^+ ion in the structure following protonation. Figure 4.2 shows a wide “u” shaped trend, but overall changes illustrated minimal exchange.

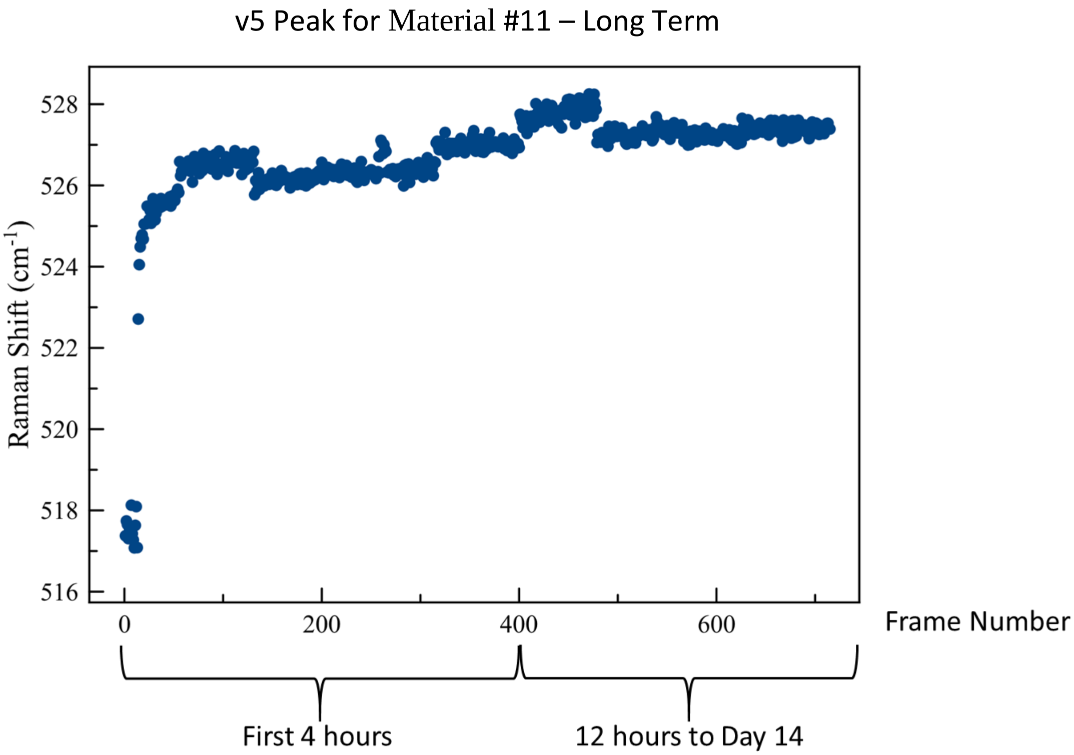

Figure 4.3 Graph showing the change in the v5 peak, which signifies distortion of the 3MR, of the K$^+$ exchange into material #3, yielding material #11. The above is the long term, two weeks, exchange experiment. Source: Created by the Author.

Figure 4.3 shows the time-resolved Raman data for the v5 peak in material #11 material. Material #11 is the K$^+$ form of material #3. The notation of long term represents a time frame of two weeks of analysis versus the standard 4 hours used in the other studies. The first 400 frames are the initial 4 hours, similar to the other exchange experiments, and the following frame numbers are comprised of 15 frames every 12 hours. As the K$^+$ ions move into the crystal structure, there is a shift to higher wave numbers in the 3MR peak. The exchange of K$^+$ into material #3 occurred nearly from frame 0 and quickly leveled off after frame 100, but exchange did continue up to frame 650 in the experiment.

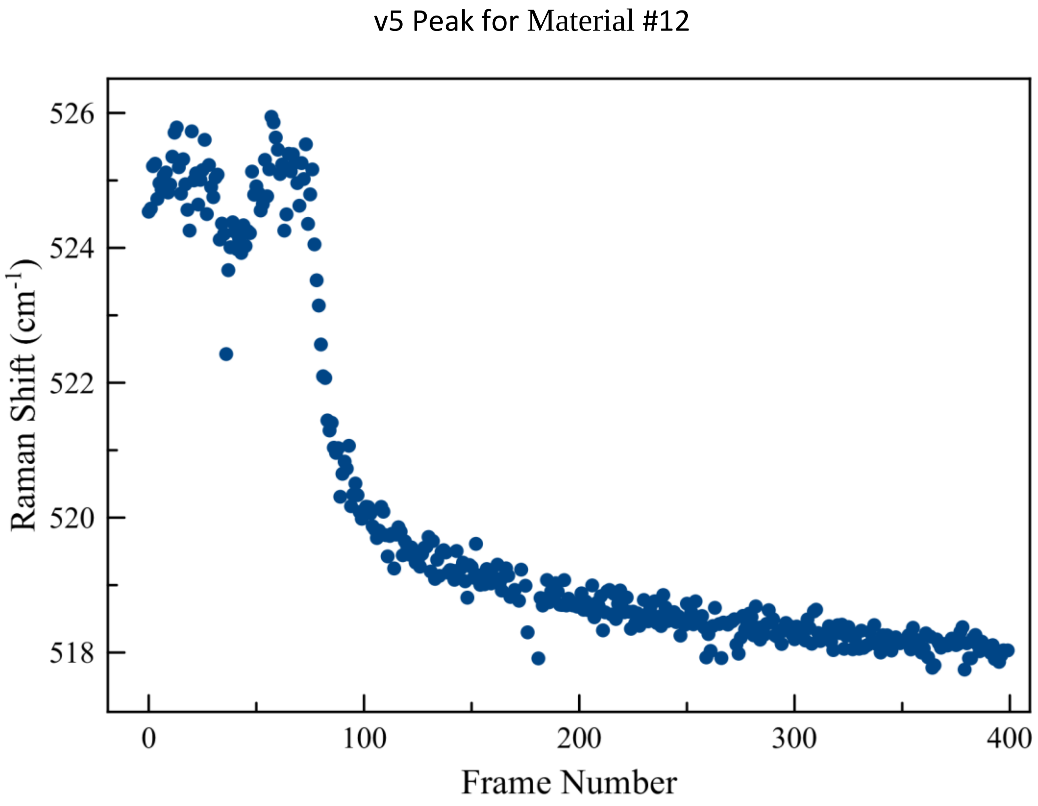

Figure 4.4 Graph showing the change in the v5 peak, which signifies distortion of the 3MR, of the Cs$^+$ exchange into material #3. Source: Created by the Author.

Figure 4.4 shows the trend of the Cs$^+$ exchange into material #3 yielding material #12. As Cs$^+$ enters into the crystal structure it causes the 3MR geometry to shift towards lower wave numbers. The v5 peak shifts from 526 cm^{-1} to 518 cm^{-1}, therefore an 8 cm^{-1} shift over the 400 frames. The trend suggests that it would continue on and level off shortly after frame 400 to reach maximum exchange seen in the last 50 to 100 frames.

XSD Studies

The XSD studies are time-resolved experiments performed at the APS Synchrotron Source. The structure of material #3 is seen in Figure 4.5 below. Due to time constraints and beam time limitations, not all of the Raman experiments were recreated at the APS. The only exchange performed with material #3 was K^+ exchange yielding material #11.

Material #3 is the maximally protonated form of material #1 and possesses more H^+ than material #2. Similar to material #1 and material #2, the H_2O sites are disordered with the monovalent extra-framework cations. The disordered H_2O sites are farther away from the cage-center toward the cage walls in material #3. The 3MR dihedral angle for the material #3 is 2.7º, a 2.7º decrease from material #1. The change in the dihedral angle is thought to be important in the variance between material #3 and material #1/material #2 in this case.

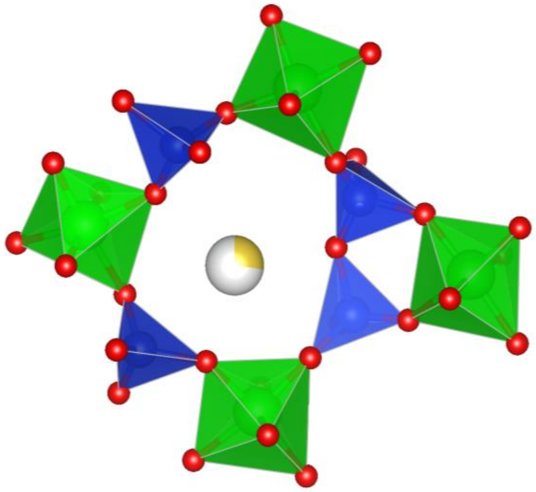

Figure 4.5 A model of the structure of material #3, with the Na^+ site in the center of the 7MR, denoted by the partially filled yellow sphere (Zr – green; Si – blue; O – red). The ZrO_6 octahedra are seen to be distorted. Source: Created by the Author.

The Na^+ site in material #3 remains in the center of the 7MR seen in Figure 4.5. The average Na-O in material #2 is 2.79Å. The unit-cell of material #3 is 12.890 (1) Å along the a-axis, therefore 2142.000 (5) $Å^3$ in volume. The unit-cell is significantly larger than that of material #1 at 12.740 (1) Å along the a-axis, with a volume of 2067.800 (5) $Å^3$, and material #2 with a volume of 2074.100 (7) $Å^3$.

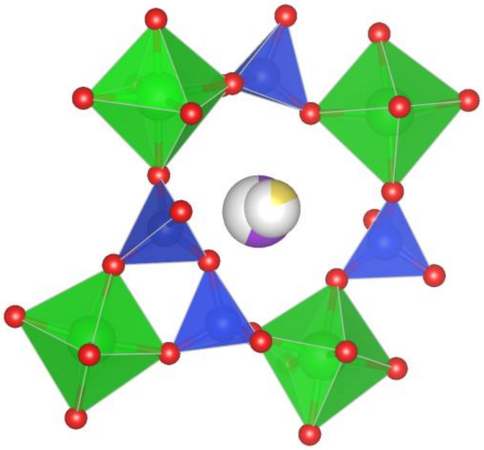

Figure 4.6 A model of the structure of material #11, with the Na^+ site in the center of the 7MR, denoted by the partially filled yellow sphere, which is in disorder with the K^+ site denoted by the purple sphere (Zr – green; Si – blue; O – red).
Source: Created by the Author.

The XSD results of the K^+ ion exchange into material #3 indicate there is a decrease in the size of the unit-cell of the material seen in Figures 4.6 and 4.7. Figure 4.6 shows a representation of the structure after it has been maximally exchanged with K^+. As seen in Figure 4.7 the unit-cell increases 0.047 Å in length. The synchrotron data illustrate that the K^+ ion resides in almost the exact same crystallographic site as the Na^+

ion. The sites are disordered with one another, with a 33% chance of Na^+ and 67% chance of K^+ occupying the extra-framework site. H_2O was evaluated and represented as O ions (Ow), which are not represented in Figure 4.6, and also occupied sites that surround the monovalent cations and are also in coordination with the framework. On either side of the cations, there is an Ow site. The average bond lengths for Na-O and K-O increased from material #3 to material #11 (2.73 Å to 2.66 Å, respectively). The torsion angle of the 3MR (Zr-O2-Si-O3) decreased significantly from material #3 to material #11 (14º to 2.7º, respectively) in this case.

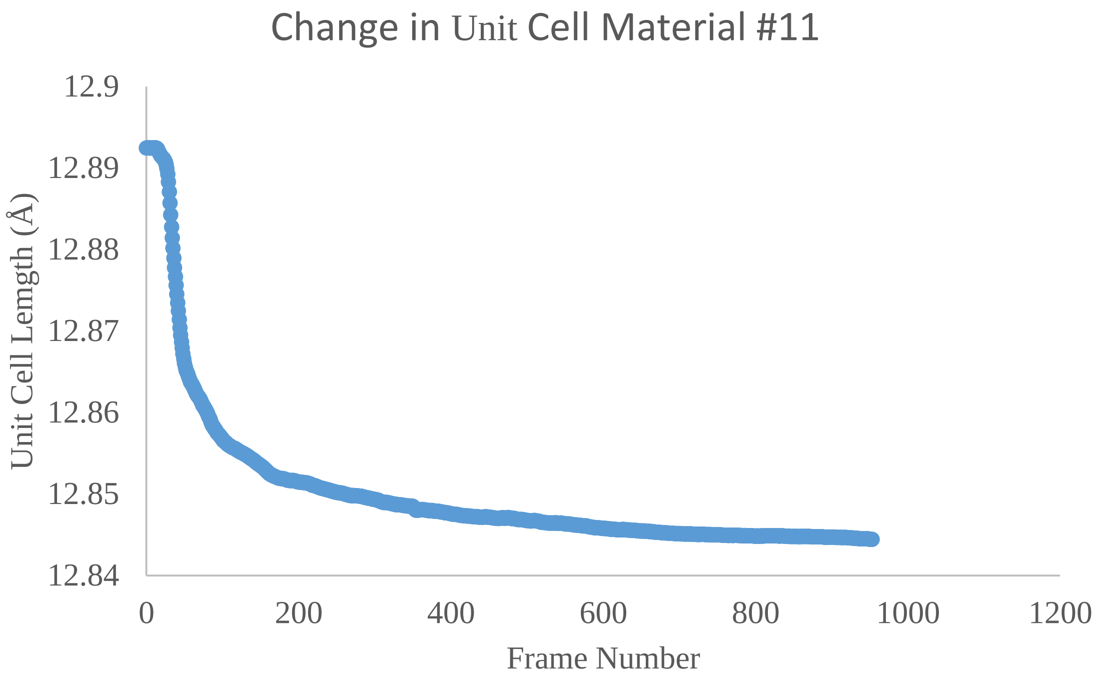

Figure 4.7 Graph showing the changes in the unit cell of material #11 through time resulting from K^+ exchange of material #3. The plot is comprised of individual points and is not a trend-line. Source: Created by the Author.

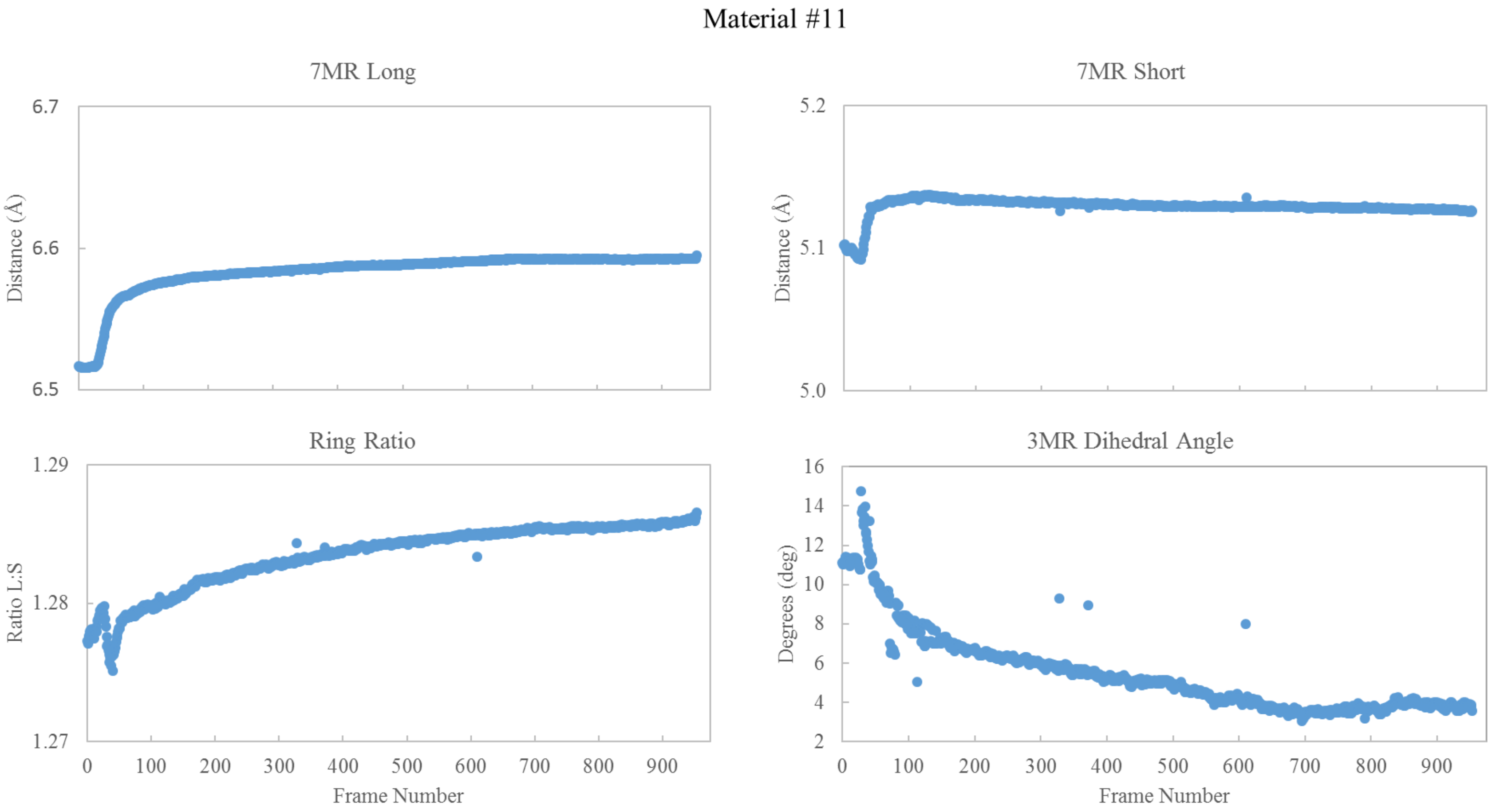

Figure 4.8 Plots represent the changes in O…O distances; O1…O3 (upper left), O2…O3 s (upper right), ratio of the O1…O3 to O2…O3 (lower left) and the changes in the torsion angle of the 3MR (lower right) in the material #11 sequential synchrotron data. Source: Created by the Author.

In the resultant material #11 (Figure 4.8), the long and short O distances remained nearly identical as time progressed with a near 0.1 Å increase in the long O1…O3, whereas the O2…O3 did not change appreciably. The ratio between the two distances increases, as the longer lengthens as the shorter remains constant. The dihedral angle, overall, drops from 14° to 2.7°, or an 11.3° change.

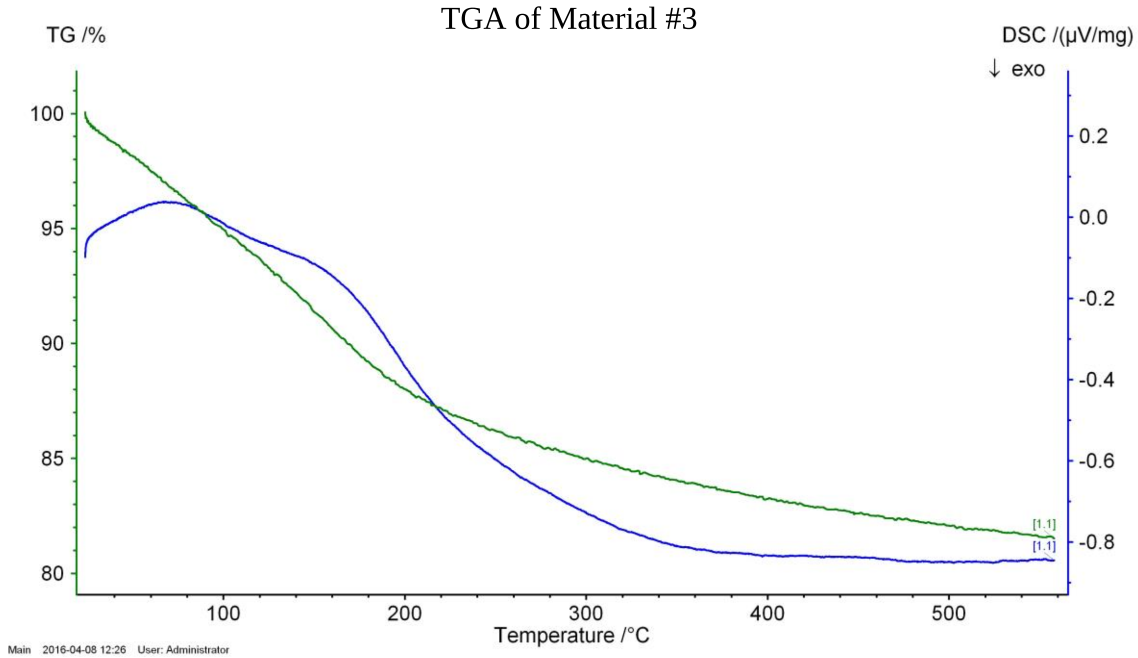

Figure 4.9 Graph showing the dehydration curve (green) and DSC curve (blue) of material #3 via TGA analysis. Source: Created by the Author.

TGA Study

The TGA was performed on the material #3 to evaluate roughly the occupancy of H_2O as an extra-framework component. There is one major dehydration event seen in Figure 4.9 above from 100 °C to 220 °C. Overall, there is about a 16% H_2O loss in the structure. The XRD analysis of the dehydrated material showed distortion and the XRD pattern (Figure 4.10) had become amorphous, due to dehydration and subsequent structure collapse.

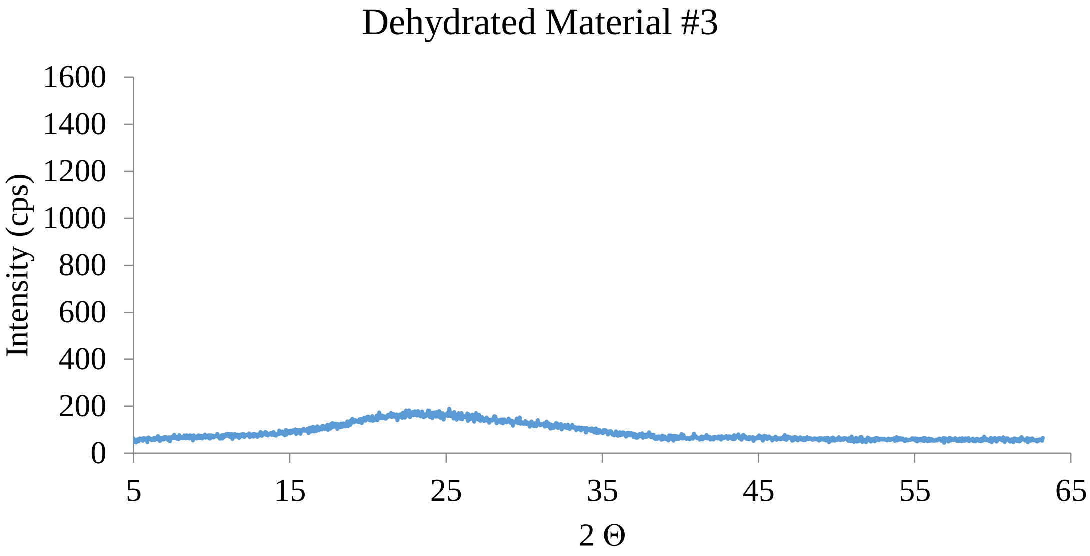

Figure 4.10 Graph showing the XRD pattern of the dehydrated material #3.
Source: Created by the Author.

Discussion

The time-resolved Raman studies showed that there is no affinity to Na$^{+,}$ when starting in the material #3 state (Figure 4.2); this suggests that, due to the increased presence of H$^+$ in the structure, Na$^+$ is unable to exchange. The K$^+$ ion exchange, as seen in Figure 4.3, and the structural information in Figure 4.6 show that the K$^+$ is able to overcome the protonation effects and enter the structure. Material #3 is maximally protonated, but a small amount of Na$^+$ still remains in the structure. As noted, the K$^+$ moves to similar site as the Na$^+$ ion, thereby causing disorder among them and the coordinated H_2O.

Cs$^+$ is able to exchange into the maximally protonated material, but shows a negative trend in the Raman shift, the opposite of K$^+$ (Figure 4.4), which signifies an elongation of the Zr-OH bond rather than shortening. The unit-cell information for the Cs$^+$ exchange was not performed at the APS, but would be a useful continuation.

Conclusion

Material #3 is the maximally protonated form of material #1. Material #3 was generated by exchanging material #1 with HCl, as discussed in Chapter 2. Material #3 was exchanged with Na^+, K^+, and Cs^+ to understand the ion exchange process and mechanisms involved during ion exchange that enable the structure to have an affinity towards K^+ over the other monovalent cations. The structural control on ion exchange in this material is the 3MR that acts to manipulate the larger 7MR and 6MR structures.

Despite the size constraints, the large Cs^+ ion was able to enter the structure as seen in the Raman spectra, albeit very slowly. It is also evident that the K^+ and Na^+ sites are nearly identical, which results in disorder among the ions when both are present. There is no affinity to Na^+ in the maximally protonated material, however the larger K^+ and Cs^+ ions were able to exchange in the Na^+ sites, suggesting that they preferred to exchange into the structure over Na^+.

Chapter 5

Role of Coordinated H_2O and Framework Protonation on Ion Selectivity, Structural Controls, and Ion Mobility in the Research Zirconosilicate Materials

Introduction

The process of utilizing ion sequestration has been demonstrated in this study and by others (Nery et al. 2003; Celestian et al. 2004) to be greatly dependent on time and the pathway channels that exist in the crystalline material of interest. The crystalline structure often needs to distort to allow exchange to occur. The mechanisms for this process are overall not well understood (Parise et al. 1998; Lee et al. 2001; Celestian et al. 2005). Hydration of crystalline structures and the protonation of the framework are thought to influence ion exchange processes. The previous chapters detailed experiments with the goal of investigating the role of both of these structural controls on the affinity of K^+ ions and the rejection of others, as well as the rate of exchange.

Table 5.1 The generated chemical formulas of the three starting materials.

Chemical Formulae	
Material #1	$Na_2ZrSi_3O_9 \cdot 2.5\ H_2O$
Material #2	$\sim HNaZrSi_3O_9 \cdot 2.8\ H_2O$
Material #3	$H_{1.3}Na_{0.7}ZrSi_3O_9 \cdot 2.5\ H_2O$

Source: Created by the Author.

Table 5.1 shows the occupancy values found in GSAS-II during the Rietveld refinements and preliminary knowledge of the research material from the Sponsor Company. Due to analytical limitations (See Chapter 1, Summary of Structure) and proprietary information, material #2 is an approximation.

Sodium Exchange

Sodium is the host cation of the research material. In material #1, Na comprises 11.2 weight percent of the structure, whereas in material #2 and material #3 it is less than half the value seen in material #1 (5.8 and 4.1 %, respectively) as calculated from the resultant formulas generated from the XSD data. In order to evaluate a preference to Na^+, the three materials were exchanged, as previously discussed. Figure 5.1 shows the comparison of the three resulting research materials. The partially protonated material #2, and maximally protonated material #3 reject the Na^+ from exchanging into the structure (material #7 and material #10). This could be attributed to the low hydration energy of Na^+ prohibiting the H_2O from being reoriented in order to overcome the $H \ldots H_2O$ bonding network in the channel. The relatively low hydration energy of Na is unable to allow Na occupancy in the hydrated channels. Material #5 is the Na^+ back exchange into material #4. This suggests a preference to Na^+ (See Chapter 2); however, it shows that the protonation effect here is too weak to prevent ion exchange and, thus, enhance ion selectivity.

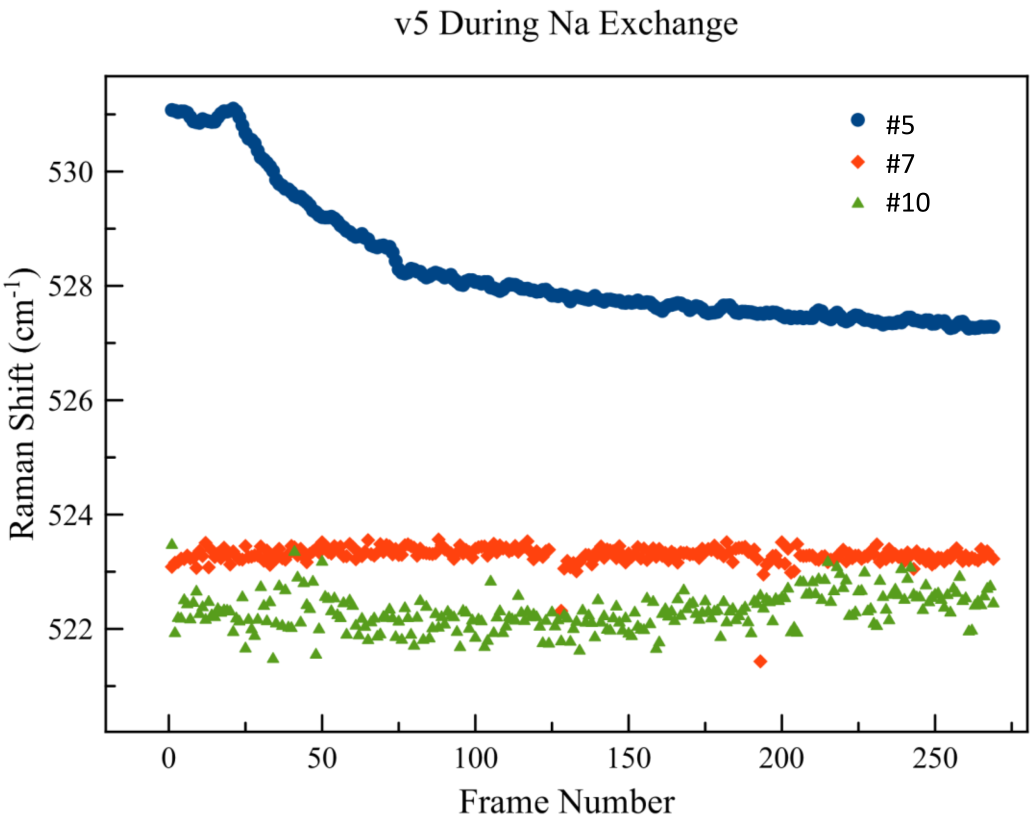

Figure 5.1 Graph showing a comparison of the three starting materials' Na$^+$ exchange experiments. The v5 peak represents changes in the 3MR geometry.
Source: Created by the Author.

Potassium and Cesium Exchange

Potassium, as the target ion, is readily able to exchange into the three starting materials evaluated in this study. Figure 5.2 shows the comparison between the Raman signals from each of the three exchanges. Material #4 (blue) is the exchanged material #1 and shows a shift to the highest wave numbers of the three exchanges. Material #8 (orange) is the exchanged material #2, which shows to have a slower rate of change than material #4, but ultimately reaches a similar level of Raman shift. Protonation can explain this slowed rate, as the K$^+$ must overcome the repulsive forces from the H$^+$ protons in order to interact with the framework; however, the maximally protonated material #3 resulting in material #11 (green and denoted as LT for long term, see Chapter 4) shows a very rapid initial rate and then levels around 527 cm^{-1}. Material #11 does not reach as high of wave numbers as material #4 and material #8, which suggests that not as many K^+ ions are able to be taken into the structure, but it does so at a faster rate.

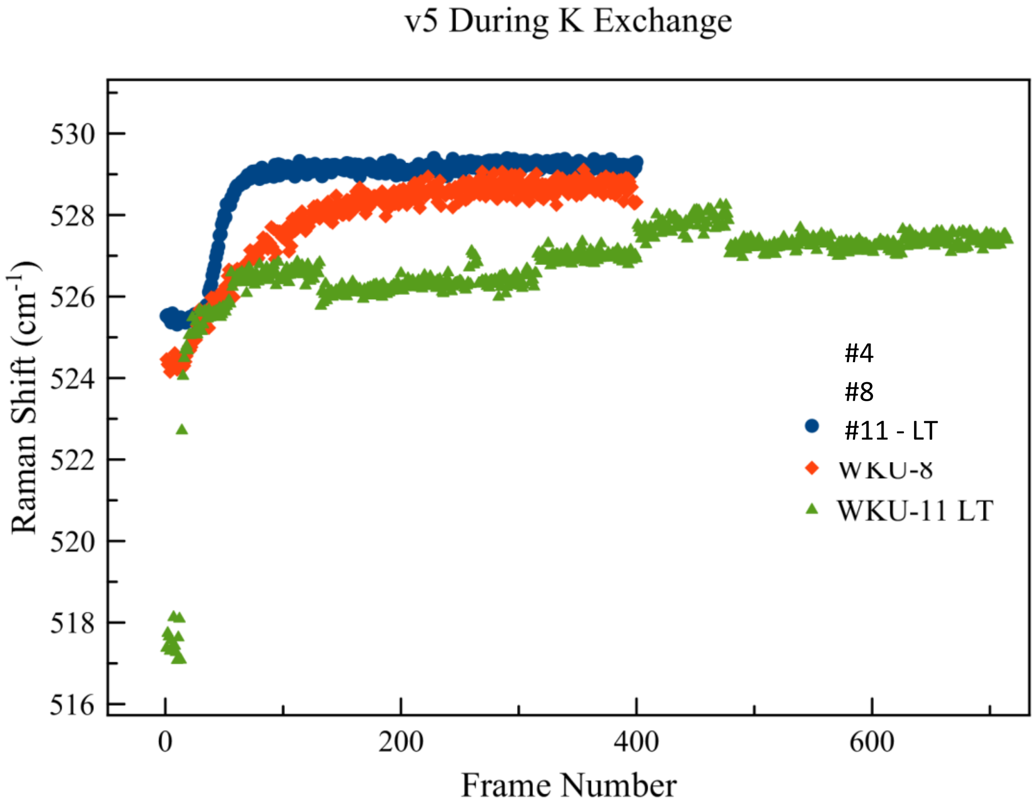

Figure 5.2 Graph showing a comparison of the three starting materials' K^+ exchange experiments. The v5 peak represents changes in the 3MR geometry.
Source: Created by the Author.

Material #11 shows a faster rate of deformation versus both material #4 and material #8. Material #4 and material #8 suggest that protonation slows ion exchange, whereas the mostly protonated form actually has the fastest rate of exchange. The role of H_2O is thought to be important in explaining why this is the case. The increased number of protons also causes an increase in the H_2O held in each starting material (Table 5.1), which may lead to a stronger H…H_2O bond network in the channels. The same effect is also seen in the exchange of Cs^+ into the three materials shown in Figure 5.3. Protonation here results in faster rates of deformation to lower wave numbers in the peaks of the Raman spectra. Material #6 and material #9 show different wave numbers for the peak position representing the 3MR distortion, but are slower than the rate for material #12. Protonation would explain the repulsion of multivalent cations; however, the monovalent cations are more likely influenced by the ring geometry and hydration energies.

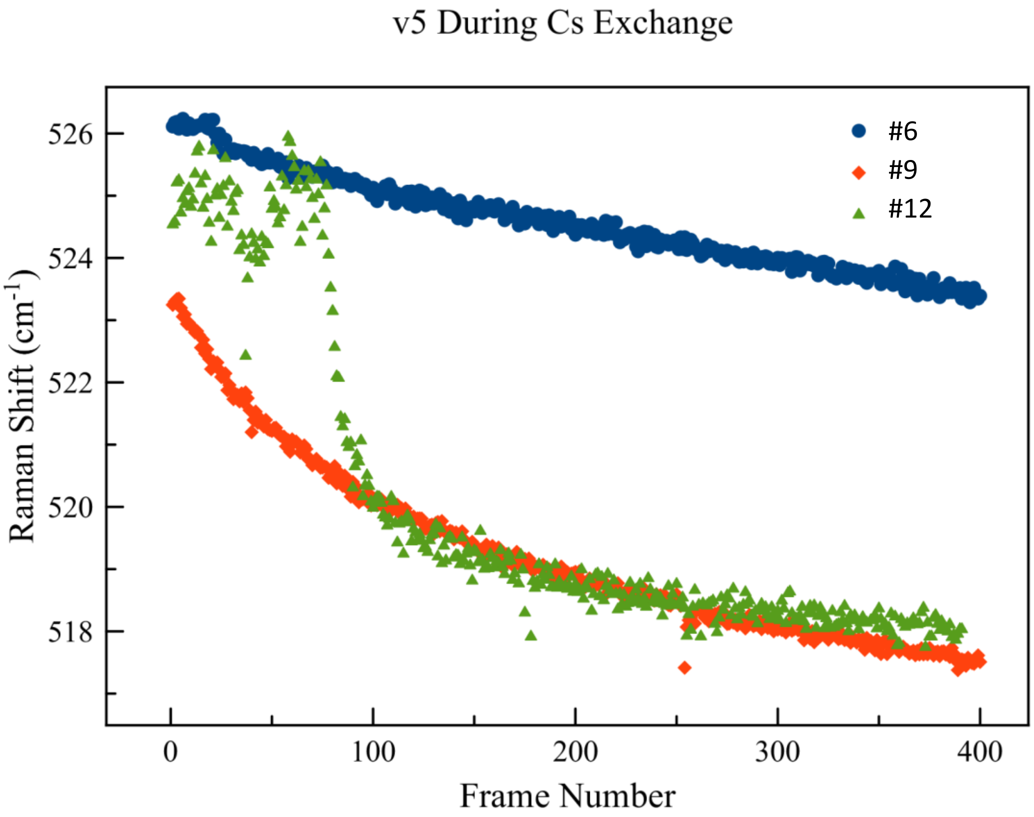

Figure 5.3 Graph showing a comparison of the three starting materials' Cs^+ exchange experiments. The v5 peak represents changes in the 3MR geometry.
Source: Created by the Author.

Structural Response due to Protonation and Hydrolysis

The changes in the unit-cell of the three starting materials, as each are exchanged with their respective ions, provides physical evidence to the protonation and hydration effects. If the unit-cell is seen to increase, then it would be evident that something is causing the structure to open up, or vice versa. Figure 5.4 shows the changes to the unit-cell in the three K^+ exchanged forms (material #4, material #8, and material #11), the maximally protonated material #3, and the Cs^+ exchanged materials, #2 and #9.

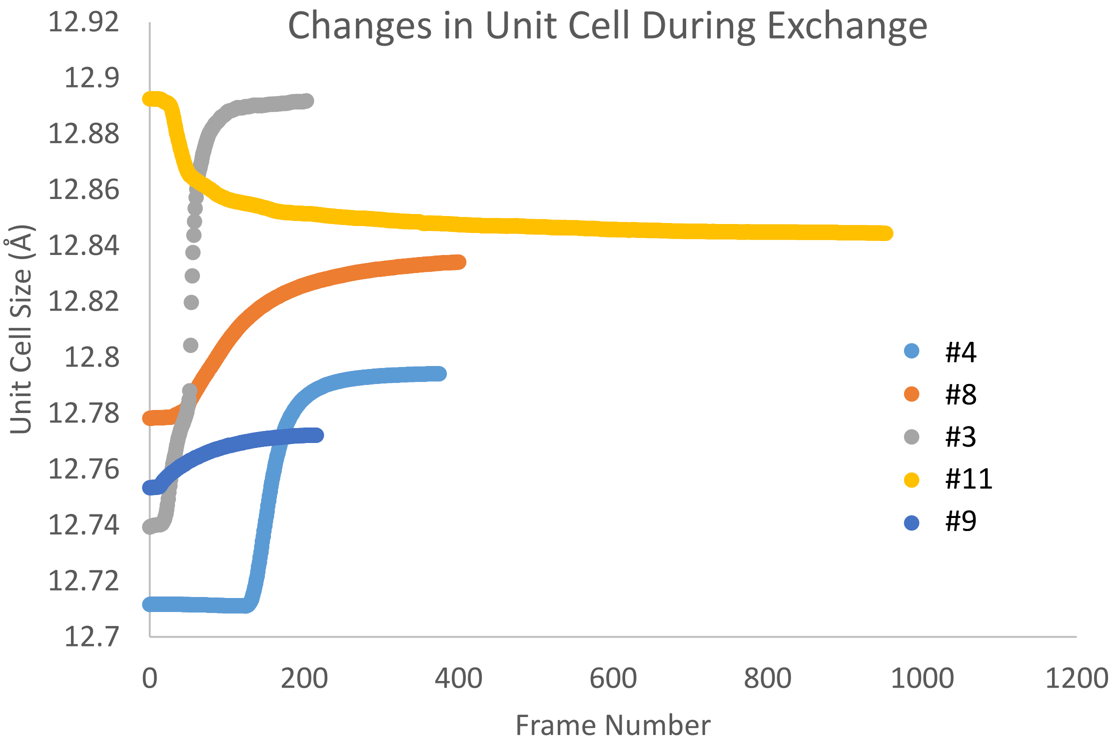

Figure 5.4 Graph showing a comparison of unit-cell size changes during H^+, K^+, and Cs^+ exchange of material #1 yielding the four noted materials discussed earlier in this paper. Source: Created by the Author.

The exchange of K^+ with material #1 and material #2 yields material #4 and material #8, respectively. Material #4 initially possesses the smallest unit-cell of 12.71 Å (2053.2 Å^3) and material #8 at 12.78Å (2087.34 Å^3). The variance in the size initially between the two forms is proton occupancy. Material #3 and material #9 should have the same initially size as material #4 and material #8, respectively, as they originate from the same materials; therefore, there is an offset error seen of $^{+}/-$ 0.02 Å in the data potentially caused by zero shift errors in sample displacement or other experimental errors. Material #3, with the highest amount of H^+, shows a significantly larger unit-cell when exchange has completed, with a final size of 12.89 Å (2141.70 $Å^3$). Material #4, material #8, and material #9 all show an increase in the unit-cell as the K^+ ion or Cs^+ exchange into the structure. These ions are larger than the original host cation, thus the structure must increase in size to allow for exchange to occur; however, with material #11 generated from material #3, it decreases in size when exchanged with K^+. This exchange also possesses the fastest rate of exchange, which is likely due to the increased size of the structure and allows the ion to pass into the structure more easily. The other forms have more deformation that needs to occur before exchange can begin and that likely hinders ion exchange in those materials.

Conclusion

The process of ion exchange and its application in industry, academics, agriculture, medicine, and others is a new way to utilize the natural properties of minerals and synthetic forms of natural materials. This body of work increases understanding of the ion exchange and sequestering process of these micro-porous materials and there is strong evidence for a vital role of H^+ and H_2O in the ability of a material to exchange ions. In this study, both the Raman microscopy results and the X-ray results reveal how the structure responds to exchange and the effects of protonation. The two methods are in good agreement and demonstrate that protonation can make the research material more selective for K^+ ions and can increase the uptake rate. The protons act like as lever that needs to be moved to allow for an ion to exchange; otherwise, the repulsive force between the two cations and the strength of the OH polar covalent bond would result in pushing the extra-framework cation out of the structure. It cannot be determined if protonation is the only reason for the increased selectivity, or if the hydration of the structure is also important. Without these coordinated H_2O molecules in the void space of the structure, they would collapse and turn amorphous, as seen in the TGA studies. Further work with neutron scattering would be needed to better evaluate the absolute positions of H^+. It was determined that the research material is effective at sequestering K^+, due to its unique structure and increased protonation/hydration activity.

References

Anker, S., Kosiborod M., Zannad, F., Piña, I., McCullough, P., Filippatos, G., Van der meer, P., Ponikowski, P., Rasmussen, H., Lavin, P., Singh, B., Yand, A., Deedwania, P. 2013. Maintenance of Serum Potassium with Sodium Zirconium Cyclosilicate (ZS-9) in Heart Failure Patients: Results from a Phase 3 Randomized, Double-Blind, Placebo-Controlled Trial. *European Journal of Heart Failure* 17(10): 1050-56.

Bish, D., Post, J. 1989. Modern Powder Diffraction. *Reviews in Mineralogy 20*. Washington, D.C.: Mineralogical Society of America

Bortun, A., Bortun, L., Clearfield, A. 1997a. Evaluation of Synthetic Inorganic Ion Exchangers for Cesium and Strontium Removal from Contaminated Groundwater and Wastewater. *Solvent Extraction and Ion Exchange* 15: 909–29.

Bortun, A., Bortun, L., Clearfield, A. 1997b. Hydrothermal Synthesis of Sodium Zirconium Silicates and Characterization of Their Properties. *Chemistry of Materials* 9: 1854-1864.

Celestian, A., Powers, M., Rader, S. 2013. In Situ Raman Spectroscopic Study of Transient Polyhedral Distortions during Cesium Ion Exchange into Sitinakite. *American Mineralogist* 98(7): 1153–61.

Celestian, A., Medvedev, D., Tripathi, A., Parise, J., Clearfield, A. 2005. Optimizing Synthesis of Na2Ti2SiO7 2H2O (Na-CST) and Ion Exchange Pathways for Cs0.4H 1.6Ti2SiO7 H2O (Cs-CST) Determined from in Situ Synchrotron X-Ray Powder Diffraction. *Nuclear Instruments and Methods in Physics Research, Section B: Beam Interactions with Materials and Atoms* 238(1–4): 61–69.

Celestian, A., Parise, J., Goodell, C., Tripathi, A., Hanson, J. 2004. Time-Resolved Diffraction Studies of Ion Exchange: K+ and Na+ Exchange into (Al, Ge) Gismondine (GIS) Na24Al24Ge24O96 Center Dot 40H(2)O and K(8)AL(8)Ge(8)O(32) · 8H(2)O. *Chemistry of Materials* 16 (11): 2244–54.

Fu, F., Wang, Q. 2011. Removal of Heavy Metal Ions from Wastewaters: A Review. *Journal of Environmental Management* 92(3): 407–18.

Galadima, A., Muraza, O. 2015. Zeolite Catalysts in Upgrading of Bioethanol to Fuels Range Hydrocarbons: A Review. *Journal of Industrial and Engineering Chemistry* 31 (August): 1–14.

Góra-Marek, K., Brylewska, K., Tarach, K., Rutkowska, M., Jablonska, M., Choi, M., Chmielarz, L. 2015. IR Studies of Fe Modified ZSM-5 Zeolites of Diverse Mesopore Topologies in the Terms of Their Catalytic Performance in NH3-SCR and NH3-SCO Processes. *Applied Catalysis B: Environmental* 179 (December): 589–98.

Helfferich, F. 1962. *Ion Exchange*. New York: McGraw-Hill.

Jones, G., Willett, P., Glen, R., Leach, A., Taylor, A. 1997. Development and Validation of a Genetic Algorithm for Flexible Docking. *Journal of Molecular Biology* 267 (3): 727–48.

Kosiborod, M., Rasmussen H., Lavin, P., Qunibi, W., Spinowitz, B., Packham, P., Roger, S., Yang, A., Lerma, E., Singh, B. 2014. Effect of Sodium Zirconium Cyclosilicate on Potassium Lowering for 28 Days Among Outpatients With Hyperkalemia. *The Journal of the American Medical Association* 312 (21): 2223-33.

Kumar D., Dipak, B., Sarmah, P. 2015. Recent Advances in Metal Nanoparticles Stabilization into Nanopores of Montmorillonite and Their Catalytic Applications for Fine Chemicals Synthesis. *Catalysis Reviews* 57 (3): 257–305.

Lee, Y, Reisner B., Hanson, J. 2001. New Insight into Cation Relocations within the Pores of Zeolite RHO: In Situ Synchrotron X-Ray and Neutron Powder Diffraction Studies of Pb- and Cd-Exchanged RHO. *The Journal of Physical Chemistry B* 105 (30): 7188–99.

Masters, B. 2009. *The Raman Effect*. New Brunswick, NJ: Rutger's University, Department of Physics. Online at: https://www.physics.rutgers.edu/grad/506/raman/raman.pdf.

Mayani, V., Mayani, S., Kim, SW. 2015. Simple Preparation of Tungsten Supported Carbon Nanoreactors for Specific Applications: Adsorption, Catalysis and Electrochemical Activity. *Applied Surface Science* 345 (August): 433–39.

Mishra, S., Tiwari, D., Prasad, S., Dubey, R., Mishra, M. 2006. Inorganic Ion-Exchangers in Radioactive Waste Management - Part XVI: Uptake of Some Metal Phosphates (Stannic and Zirconium) for Cs-134. *Journal of Radioanalytical and Nuclear Chemistry* 268: 191–99.

Momma, K., Izumi, F. 2011. VESTA 3 for Three-Dimensional Visualization of Crystal, Volumetric and Morphology Data. *Journal of Applied Crystallography* 44: 1272–76.

Mumpton, F. 1999. La roca magica: uses of natural zeolites in agriculture and industry. *Procedings of the National Academy of Science* 96: 3463–70.

Nery, J., Mascarenha, Y., Cheetham, A. 2003. A Study of the Highly Crystalline, Low-Silica Fully Hydrated Zeolite P Ion Exchanged with (Mn2+, Cd2+, Pb2+, Sr2+, Ba2+) Cations. *Microporous and Mesoporous Materials* 57(3): 229–48.

Packham, D., Kosiborod, M. 2015. Potential New Agents for the Management of Hyperkalemia. *American Journal of Cardiovascular Drugs* 16(1). 19–31.

Packham, D., Rasmussen, H., Lavin, P., El-Shahawy, M., Roger, S., Block, G., Qunibi, W., Pergola, P., Singh, B. 2014. Sodium Zirconium Cyclosilicate in Hyperkalemia. *The New England Journal of Medicine* 372(3): 222–31.

Pang, W., Yu, J., Huo, Q. 2007. *Chemistry of Zeolites and Related Porous Materials: Synthesis and Structure*. New York: John Wiley and Sons.

Parise, J.B., Cahill, C., Chen, J. 1998. Rietveld Refinement Using Time-Resolved Data. *Abstracts of Papers of the American Chemical Society* 215: U811.

Rafique, Z., Peacock, W., LoVecchio, F., Levy, P. 2015. Sodium Zirconium Cyclosilicate (ZS-9) for the Treatment of Hyperkalemia. *Expert Opinion on Pharmacotherapy* 16 (11): 1727–34.

Shannon, R.D., Prewitt, C.T. 1969. Effective Ionic Radii in Oxides and Fluorides. *Acta Crystalography* B25(1454): 925-946.

Simon, V., Thuret, A., Candy, L., Bassil, S., Duthen, S., Raynaud, C., Masseron, A. 2015. Recovery of Hydroxycinnamic Acids from Renewable Resources by Adsorption on Zeolites. *Chemical Engineering Journal* 280 (November): 748–54.

Stavros, F., Yang, A., Leon, A., Nuttall, M., Rasmussen, H. 2014. Characterization of Structure and Function of ZS-9, a K+ Selective Ion Trap. *PloS One* 9 (12): e114686.

Toby, B., Von Dreele, R. 2013. GSAS-II: The Genesis of a Modern Open-Source All Purpose Crystallography Software Package. *Journal of Applied Crystallography* 46 (2): 544–49.

Uguina, M.A., Delgado, J.A., Águeda, V.I., García-Sanz, A. 2008. Zeolites and Related Materials: Trends, Targets and Challenges. *Proceedings of the 4th International FEZA Conference*. *Studies in Surface Science and Catalysis* 174(Part A): 155-60.

Watson, M., Abbott, K., Yuan, C. 2010. Damned If You Do, Damned If You Don’t: Potassium Binding Resins in Hyperkalemia. *Clinical Journal of the American Society of Nephrology* 5(10): 1723–26.